RESEARCH ARTICLE

WILEY

A unified CFD-DEM approach for modeling of debris flow impacts on flexible barriers

Xingyue Li | Jidong Zhao [iD]

Department of Civil and Environmental Engineering, Hong Kong University of Science and Technology, Hong Kong

Correspondence
Jidong Zhao, Department of Civil and Environmental Engineering, Hong Kong University of Science and Technology, Hong Kong.
Email: jzhao@ust.hk

Summary

This paper presents a unified modeling framework to investigate the impacts of debris flow on flexible barriers, based on coupled computational fluid dynamics and discrete element method (CFD-DEM). We consider a debris flow as a mixture of fluid and particles where the fluid and particle phases are modeled by the CFD and the DEM, respectively. The fluid-particle coupling is considered by the exchange of interaction forces between CFD and DEM calculations. The flexible barrier is simulated by the DEM as a network of bonded particles with remote interactions. The proposed coupled CFD-DEM approach enables us to conveniently handle the complicated three-way interactions among the fluid, the particles, and the flexible barrier structure for debris flow impact simulations. The proposed approach is first used to investigate the influences of channel inclination and the volumetric solid fraction in a debris mixture on the impact force, the resultant deformation, and the retained mass in a flexible barrier. The predictions agree well with existing experimental and numerical studies. We further examine the possible failure modes of a flexible barrier under debris flow impact and their underlying mechanisms. The performance of different components in a flexible barrier system, including single wires, double twists and cables, and their load sharing mechanisms, are carefully evaluated. The proposed unified framework offers a novel, promising pathway towards physically based, quantitative analysis and design of flexible barriers for debris flow mitigation.

KEYWORDS
coupled CFD-DEM, debris flow, discrete modeling, flexible barrier, particle-fluid-barrier interactions

1 | INTRODUCTION

Rigid barriers are widely used worldwide for debris flow mitigation. The use of flexible barriers has become increasingly popular in recent years. Compared with traditional rigid barriers, flexible barriers are easy and economical for installations and replacements, especially in inaccessible mountainous regions where debris flows occur frequently. In urban areas, flexible barriers are also popular for debris-resisting since their presence is not excessively intrusive for the surrounding environment.[1,2] Although the design of rigid barriers has accumulated rich engineering experience, it cannot be directly applied to the design of flexible barriers, due to totally different mechanical characteristics of the two. When a debris flow impacts on a flexible barrier, intricate multiway interactions between the debris and the highly deformable barrier structure may occur, which are extremely complicated and challenging to characterize. Integrated considerations of the debris flow and flexible barrier are needed. No firm guidelines built upon sounded theoretical basis

are available for flexible barrier design. Only limited experimental and numerical studies have been reported recently.[1,3,4] Reliable characterization and modeling of debris flow and its impacts on a flexible barrier hinge on realistic consideration of the three-way coupling and interactions among the debris fluid, the debris solid and the flexible barrier structure. Meanwhile, the failure of a flexible barrier, when subjected to debris flow impacts, being a key aspect for design, is rarely investigated due to various practical limitations and challenges.[5,6] In practice, nonuniform flexible barriers with various reinforcements including cables have commonly been adopted.[4] Their individual and collective performances in field applications may differ significantly from those observed from small-scale tests and simplified numerical simulations (eg, based on uniform barriers).[1,7] A robust predictive numerical/analytical tool that can take into account all these aspects is urgently needed for practical design but unavailable to date.

In this study, we present a unified, novel discrete-based numerical approach to model the complicated impacts of debris flow on a flexible barrier. Specifically, we use a coupled computational fluid dynamics and discrete element method (CFD-DEM) approach to simulate the debris flow as a mixture of viscous fluid and a particulate system consisting of frictional grains that interact with one another through frictional contacts and dissipative collisions.[8-10] Key to the coupling is the exchange of interaction forces between CFD and DEM computations to consider the complicated fluid-particle interactions in a debris flow. As mentioned, a particular challenge in debris flow simulation is to further model its impact on a flexible barrier. In this connection, we exploit the flexibility of the discrete element method and its latest progresses in modeling rockfall fence,[11,12] and model a flexible barrier as a bonded particle network with remote interactions by DEM. In this way, the so-called three-way interactions (fluid, particle, and barrier) can be seamlessly considered in our coupled CFD-DEM approach without resorting to complicated third-party coupling such as FEM (eg, Leonardi et al[1]). Our approach helps to realistically capture the possible failure modes of flexible barrier caused by debris impacts, and to evaluate the performance of different components in a flexible barrier and mechanisms of a flexible barrier during the impact of a debris flow. With further validations, the proposed approach may serve as a new-generation numerical tool for future design and analysis of debris-resisting flexible structures.

2 | METHODOLOGY

2.1 | Coupled CFD-DEM for debris flow modeling

2.1.1 | DEM modeling of particle system

The DEM[13] is used to model the particle system in a debris mixture. DEM solves the following Newton's equation governing the translational and rotational motions of each particle i in the particle system:

$$\begin{cases} m_i \dfrac{d\boldsymbol{U}_i^p}{dt} = \sum_{j=1}^{n_i^c} \boldsymbol{F}_{ij}^c + \boldsymbol{F}_i^f + \boldsymbol{F}_i^g \\ I_i \dfrac{d\boldsymbol{\omega}_i}{dt} = \sum_{j=1}^{n_i^c} (\boldsymbol{M}_{t,ij} + \boldsymbol{M}_{r,ij}), \end{cases} \tag{1}$$

where m_i and I_i are the mass and moment of inertia of particle i. $\boldsymbol{U}_i^p$ and $\boldsymbol{\omega}_i$ denote the translational and angular velocities of particle i, respectively. n_i^c is the number of total contacts for particle i. $\boldsymbol{F}_{ij}^c$ is the contact force acting on particle i by particle j or walls. $\boldsymbol{F}_i^f$ is the particle-fluid interaction force acting on the particle, which includes the drag force and the buoyancy force. $\boldsymbol{F}_i^g$ is the gravitational force of particle i. $\boldsymbol{M}_{t,ij}$ and $\boldsymbol{M}_{r,ij}$ are the torques acting on particle i by the tangential force and the rolling friction force, respectively.

The particles considered in this study are assumed to be rigid spheres and are free to roll. While rolling resistance can be important to account for the effect of non-spherical particles, it can be considered by a rolling resistance model (see, eg, Li and Zhao[14]). However, rolling resistance is not considered in this study to reduce model complexity.

The contact force $\boldsymbol{F}_{ij}^c$ is calculated as follows based on Hertzian-Mindlin contact law as illustrated in Figure 1:

$$\boldsymbol{F}_{ij}^c = \left(k^n \delta_{ij}^{\boldsymbol{n}} - \gamma^n v_{ij}^{\boldsymbol{n}} \right) + \left[\left(\boldsymbol{F}_{spring}^{s0} + k^s \Delta \delta_{ij}^{\boldsymbol{t}} \right) - \gamma^s v_{ij}^{\boldsymbol{t}} \right], \tag{2}$$

where the terms on the right hand side refer to the normal spring force, the normal damping force, the shear spring force and the shear damping force, respectively. The total tangential force is the sum of shear spring force and shear damping force, denoted by the term in the square bracket. It increases until the shear spring force $\boldsymbol{F}_{spring}^s$
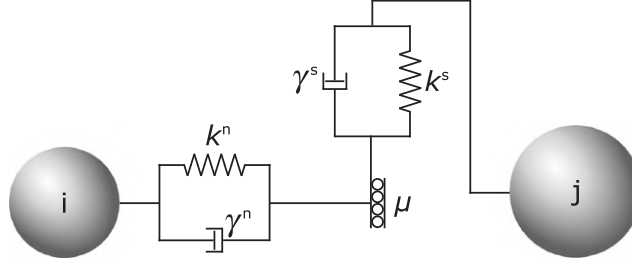
FIGURE 1 Schematic of the Hertzian-Mindlin contact law used in the DEM simulation and the model parameters used (the normal and tangential stiffness: k^n and k^s; the damping coefficients for normal and tangential contacts: γ_n and γ_s; friction coefficient μ)

(ie, $\boldsymbol{F}^{s0}_{spring} + k^s \Delta\delta^{\boldsymbol{t}}_{ij}$) reaches $\mu\boldsymbol{F}^n$, where μ is the friction coefficient and $\boldsymbol{F}^n$ is the total normal force in the first parenthesis. The tangential spring force is then held at $\boldsymbol{F}^s_{spring} = \mu\boldsymbol{F}^n$ until the particles lose contact. $\boldsymbol{F}^{s0}_{spring}$ is the initial tangential spring force at the previous time step. k^n and k^s are the normal and tangential stiffnesses, respectively. $\delta^{\boldsymbol{n}}_{ij}$ is the overlap distance in the normal direction and $\Delta\delta^{\boldsymbol{t}}_{ij}$ is the incremental tangential displacement. γ^n and γ^s are the damping coefficients in the normal and tangential directions of the contact, respectively. $v^{\boldsymbol{n}}_{ij}$ and $v^{\boldsymbol{t}}_{ij}$ are the normal and tangential components of the relative velocity of the overlapped two particles. Given the mass, radius, Young's modulus and Poisson's ratio of each of the two contacting particles and the coefficient of restitution between them, the normal and tangential stiffness (k^n and k^s) as well as the damping coefficients (γ^n and γ^s) can be calculated by the following equations:

$$k^n = \frac{4}{3}E^*\sqrt{R^*\delta^{\boldsymbol{n}}_{ij}}, \tag{3}$$

$$k^s = 8G^*\sqrt{R^*\delta^{\boldsymbol{n}}_{ij}}, \tag{4}$$

$$\gamma^n = -2\sqrt{\frac{5}{6}}\beta\sqrt{S_n m^*} \geqslant 0, \tag{5}$$

$$\gamma^s = -2\sqrt{\frac{5}{6}}\beta\sqrt{S_t m^*} \geqslant 0, \tag{6}$$

where $\dfrac{1}{E^*} = \dfrac{(1-v_i^2)}{E_i} + \dfrac{1-v_j^2}{E_j}$; $\dfrac{1}{G^*} = \dfrac{2(2-v_i)(1+v_i)}{E_i} + \dfrac{2(2-v_j)(1+v_j)}{E_j}$; $\dfrac{1}{R^*} = \dfrac{1}{R_i} + \dfrac{1}{R_j}$; $\dfrac{1}{m^*} = \dfrac{1}{m_i} + \dfrac{1}{m_j}$; $S_n = 2E^*\sqrt{R^*\delta^{\boldsymbol{n}}_{ij}}$;

$S_t = 8G^*\sqrt{R^*\delta^{\boldsymbol{n}}_{ij}}$; $\beta = \dfrac{ln(e)}{\sqrt{ln^2(e) + \pi^2}}$. E_i and E_j are the Young's moduli of two contacting particles i and j. v_i and v_j are the Poisson's ratios of particle i and particle j. R_i and R_j are the radii of the contacting particles. m_i and m_j are the masses of the contacting particles. e is the coefficient of restitution. The contact behavior between a particle i and a wall follows the same law described above, where the wall is regarded to be a particle with infinite radius and mass.

2.1.2 | CFD modeling of the fluid system

The fluid in a debris mixture is simulated by the CFD. The fluid domain is discretized into fluid cells. For each fluid cell, CFD solves the following continuity equation and the locally averaged Navier-Stokes equation:

$$\begin{cases} \dfrac{\partial \varepsilon_f \rho_f}{\partial t} + \nabla \cdot (\varepsilon_f \rho_f \boldsymbol{U}^f) = 0 \\ \dfrac{\partial (\varepsilon_f \rho_f \boldsymbol{U}^f)}{\partial t} + \nabla \cdot (\varepsilon_f \rho_f \boldsymbol{U}^f \boldsymbol{U}^f) = -\nabla p - \boldsymbol{f}^p + \varepsilon_f \Delta \cdot \tau + \varepsilon_f \rho_f \boldsymbol{g}, \end{cases} \tag{7}$$

where ε_f denotes the void fraction (porosity). ρ_f is the averaged fluid density. $\boldsymbol{U}^f$ and p are the fluid velocity and pressure, respectively. $\boldsymbol{f}^p$ is the volumetric interaction force acting on the fluid by the particles within each cell. τ is

the stress tensor. The fluid is assumed to be continuous and incompressible. The fluid properties are constant within each fluid cell.

2.1.3 | Fluid-particle interaction forces

In the coupling scheme, the fluid-particle interactions in a debris mixture are considered by the exchange of interaction forces between the CFD and DEM computations. The following two interaction forces, the buoyancy force $\boldsymbol{F}^b$ and the drag force $\boldsymbol{F}^d$, are considered[15,16]:

$$\boldsymbol{F}^b = \frac{1}{6}\pi\rho_f d_p^3 \boldsymbol{g}, \tag{8}$$

where d_p is the diameter of the considered particle.

$$\boldsymbol{F}^d = \frac{\boldsymbol{U}^p \beta}{\varepsilon_p}(\boldsymbol{U}^f - \boldsymbol{U}^p), \tag{9}$$

where ε_p denotes the volume fraction of particles in the cell, which is equal to $1 - \varepsilon_f$; β denotes the inter-phase momentum transfer coefficient due to drag:

$$\beta = \frac{18\mu_f \varepsilon_f^2 \varepsilon_p}{d_p^2}\left(F_0(\varepsilon_p) + \frac{1}{2}F_3(\varepsilon_p)Re_p\right), \tag{10}$$

where

$$F_3(\varepsilon_p) = 0.0673 + 0.212\varepsilon_p + \frac{0.0232}{\varepsilon_p^5}. \tag{11}$$

If $\varepsilon_p < 0.4$,

$$F_0(\varepsilon_p) = \frac{1 + 3\sqrt{\frac{\varepsilon_p}{2}} + \frac{135}{64}\varepsilon_p\ln(\varepsilon_p) + 16.14\varepsilon_p}{1 + 0.681\varepsilon_p - 8.48\varepsilon_p^2 + 8.16\varepsilon_p^3}. \tag{12}$$

If $\varepsilon_p \geqslant 0.4$,

$$F_0(\varepsilon_p) = \frac{10\varepsilon_p}{\varepsilon_f^3}. \tag{13}$$

The Reynolds number for a particle is calculated by

$$Re_p = \frac{\varepsilon_f \rho d_p |\boldsymbol{U}^f - \boldsymbol{U}^p|}{\mu_f}, \tag{14}$$

where μ_f is the averaged viscosity of the fluid cell. Note that Equation 9 denotes the Koch-Hill model[15] which is commonly used in the modeling of fluid-particle interaction.[17] The model can provide consistent predictions with both empirical relations and experimental data.[18,19] In this study, we neglect other interaction forces, such as virtual mass force, Basset force and lift force. These forces may be important in highly unsteady flows.[17]

2.2 | DEM simulation of flexible barrier

Indeed, the coupled CFD-DEM approach enables us to simulate the flexible barrier in a unified manner, specifically, by a modified method for DEM. To simulate the wire mesh for a flexible barrier, discrete particles with remote interactions originally proposed for modeling rockfall protection fence by metallic wire meshes[11,12,20] are used. Take a hexagonal shaped wire mesh as shown in Figure 2A as example. The mechanical response of a hexagonal wire net depends on its consisting single and/or double-twist wires. To simulate such a net in DEM, 3 typical numerical steps are followed[12]:
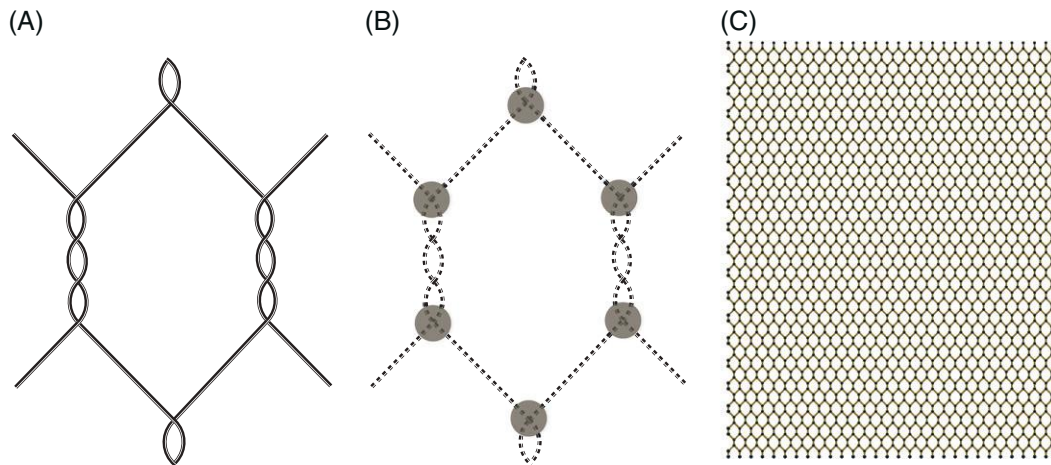
FIGURE 2 A, Illustration of simulating a double-twist wire net; B, discrete particles with remote interactions; C, discrete network for a flexible barrier formed by (B) in the DEM [Colour figure can be viewed at wileyonlinelibrary.com]

(1) A real wire is first idealized into a numerical mesh with a set of spherical particles placed at the physical nodes of the wire mesh. All particles in the mesh are assumed to be identical in size. The total physical mass of the wire mesh is assumed to lump over these particles, according to which their density is adjusted. For example, the diameter and the density of particles in the mesh used in Thoeni et al[21] are 10.8 *mm* and 5300 *kg/m*^{3}, respectively, which are the references for the diameter 10 *mm* and the density 5300 *kg/m*^{3} adopted in our study. Individually, any of these particles in the mesh can interact with the debris particles and debris fluid according to the same manner described in the foregoing subsection. Within the barrier mesh, however, these spherical particles are assumed having no physical contacts, a deviating point from the conventional way in most DEM simulations (such as for the debris particles simulation described in Section 2.1). Instead, the concept of remote interactions is used to represent the connections between neighboring nodes by a single or double-twist wire.

(2) A remote interaction refers to a virtual bar-like parallel bond used to connect two neighboring particles (as shown in Figure 3). With an equal geometric length of the corresponding wire in the real wire mesh, the bond is assumed to be weightless but can sustain both forces and moments. The term "parallel bond" is used to distinguish it from another kind of bond, "contact bond," which can only sustain forces.[22] Five parameters are used to define a parallel bond: the normal and shear stiffnesses per unit area, $\overline{k}^n$ and $\overline{k}^s$; the tensile and shear strengths, $\overline{\sigma}_c$ and $\overline{\tau}_c$; and the bond-radius multiplier $\overline{\lambda}$. The radius of a parallel bond $\overline{R}$ is calculated by
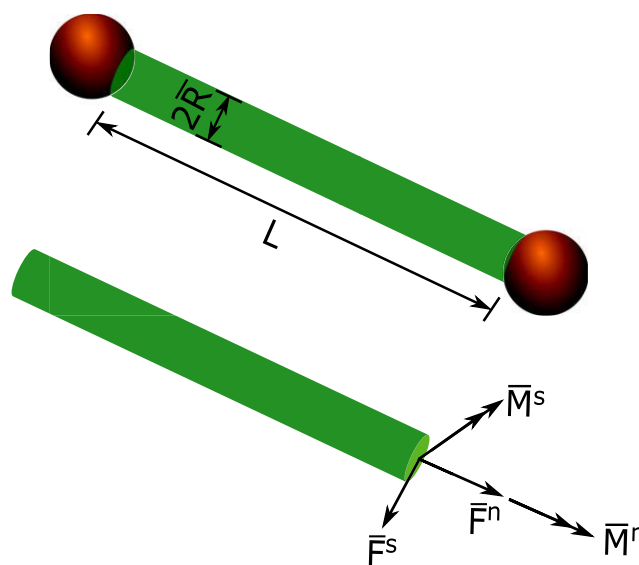
FIGURE 3 A parallel bond describing the remote interaction between particles in the barrier mesh [Colour figure can be viewed at wileyonlinelibrary.com]

$$\overline{R} = \overline{\lambda} min(R^A, R^B), \tag{15}$$

where R^A and R^B are radii of two remotely connected particles. For simplicity, in this study, identical values are adopted for the normal and shear stiffnesses; the tensile strength and shear strength are set to be equal as well; and the bond-radius multiplier $\overline{\lambda}$ is fixed to 1. Consequently, only two variables need to be specified in the subsequent simulations, namely, the bond stiffness and the bond strength. Nevertheless, the following theoretical descriptions still retain the distinctions between stiffnesses and strengths in the normal and tangential directions. Referring to Figure 3, the total force and moment sustained by a parallel bond can be expressed as $\overline{F}_i$ and $\overline{M}_i$.

$$\overline{F}_i = \overline{F}^n n_i + \overline{F}^s t_i, \tag{16}$$

$$\overline{M}_i = \overline{M}^n n_i + \overline{M}^s t_i, \tag{17}$$

where $\overline{F}^n, \overline{F}^s$ and $\overline{M}^n, \overline{M}^s$ denote the axial and shear-directed forces and moments, respectively, and n_i and t_i are the unit vectors in axial and shear directions. The initial values for $\overline{F}_i$ and $\overline{M}_i$ are set to zero. Once the loads are applied (which can be both gravity force and impacting forces), each subsequent relative displacement and rotation increment ($\Delta U^n, \Delta U^s, \Delta\theta^n, \Delta\theta^s$) produces an increment of elastic force and moment as follows which are augmented to their previous values:

$$\Delta\overline{F}^n = \overline{k}^n A \Delta U^n, \tag{18}$$

$$\Delta\overline{F}^s = -\overline{k}^s A \Delta U^s, \tag{19}$$

$$\Delta\overline{M}^n = -\overline{k}^s J \Delta\theta^n, \tag{20}$$

$$\Delta\overline{M}^s = -\overline{k}^n I \Delta\theta^s, \tag{21}$$

where A, I, and J are respectively the area, moment of inertia and polar moment of inertia of the parallel bond cross-section defined by $A = \pi\overline{R}^2$, $I = 0.25\pi\overline{R}^4$ and $J = 0.5\pi\overline{R}^4$.

The maximum tensile and shear stresses acting on the parallel-bond periphery are derived from the beam theory in structural mechanics as follows:

$$\overline{\sigma}^{max} = \frac{-\overline{F}^n}{A} + \frac{|\overline{M}^s|\overline{R}}{I}, \tag{22}$$

$$\overline{\tau}^{max} = |\frac{\overline{F}^s|}{A} + |\frac{\overline{M}^n|\overline{R}}{J}. \tag{23}$$

If the maximum tensile stress exceeds the tensile strength (ie, $\overline{\sigma}^{max} \geqslant \overline{\sigma}_c$) or the maximum shear stress exceeds the shear strength (ie, $\overline{\tau}^{max} \geqslant \overline{\tau}_c$), the parallel bond is assumed to break. It is worth noting that the parallel bond model here simulates the breaking of an individual wire as a typical elastic brittle failure. With proper calibrated elastic stiffness and bonding strength, the model can indeed produce large stretching with brittle failure, matching the plastic behavior a metal wire can typically experience.

(3) A final step is to calibrate the model parameters for the single wire and/or double twist wires and apply them to the corresponding virtual wires in the numerical mesh. As mentioned, all mass in the numerical mesh are to be lumped to the particles only; therefore, the parallel bonds represent virtual wires which are deformable and breakable.

With the above consideration, the same DEM code of a coupled CFD-DEM approach can be easily adapted to accommodate the particles with remote interactions for simulating the wire mesh. More importantly, the interaction between the flexible barrier and the debris solid can be easily executed under the same umbrella of DEM through contacts among the debris particles and the wire mesh particles according to the same contact laws in usual DEM.

Meanwhile, the interaction between the flexible barrier and the fluid in the debris mixture can be considered in exactly the same manner as described in Section 2.1, as if the flexible mesh particles were the same as particles in the debris mixture. Note that in the present framework, no direct interaction is considered for the virtual wires (parallel bonds) with either the particles or the fluid in the debris mixture. Furthermore, other supplementary elements for the flexible barrier, such as reinforcing cables, can also be readily modeled by the DEM and implemented into the framework by directly adding extra bonds between particles in the barrier net to mimic the attached cables on the barrier net as illustrated in the field.[3] Consequently, the proposed CFD-DEM approach offers a unified framework for us to handle the three-way interactions among the debris solids, the debris fluid, and the flexible barrier mesh. We also note that there have been studies based on DEM to simulate interactions between dry granular particles/boulders and wire fences, for applications in either debris flow or rock fall engineering.[20,23-27] The present study will highlight that the consideration of debris fluid plays a key role in realistic simulation of debris flow as well as its interaction with flexible barriers.

3 | SIMULATION RESULTS AND DISCUSSION

This section presents the modeling and results for a debris flow impacting on a flexible barrier based on the proposed coupled CFD-DEM approach. Three groups of simulations are analyzed to verify the predictions on debris flow by the coupled CFD-DEM approach, two for varied slope angles and solid contents in the mixture for general trend observations, and the third on a uniform wire mesh with supporting cables where experimental data are available for comparison. The predictive capability of the coupled CFD-DEM method in modeling the debris flow impacting on flexible barriers is then demonstrated. In particular, different possible failure patterns caused by debris impacting on a uniform barrier are carefully examined. A parametric study is further conducted on the effects of bond strength and bond stiffness in a barrier on the maximum sustained force of the barrier.

3.1 | Model setup for debris mixture and flexible barrier

Figure 4 illustrates the model setup of a debris mixture and a flexible barrier constructed on an inclined slope with slope angle of θ. The simulation domain is bounded by 6 boundary faces $F_1 - F_6$. A cubic mixture of soil particles
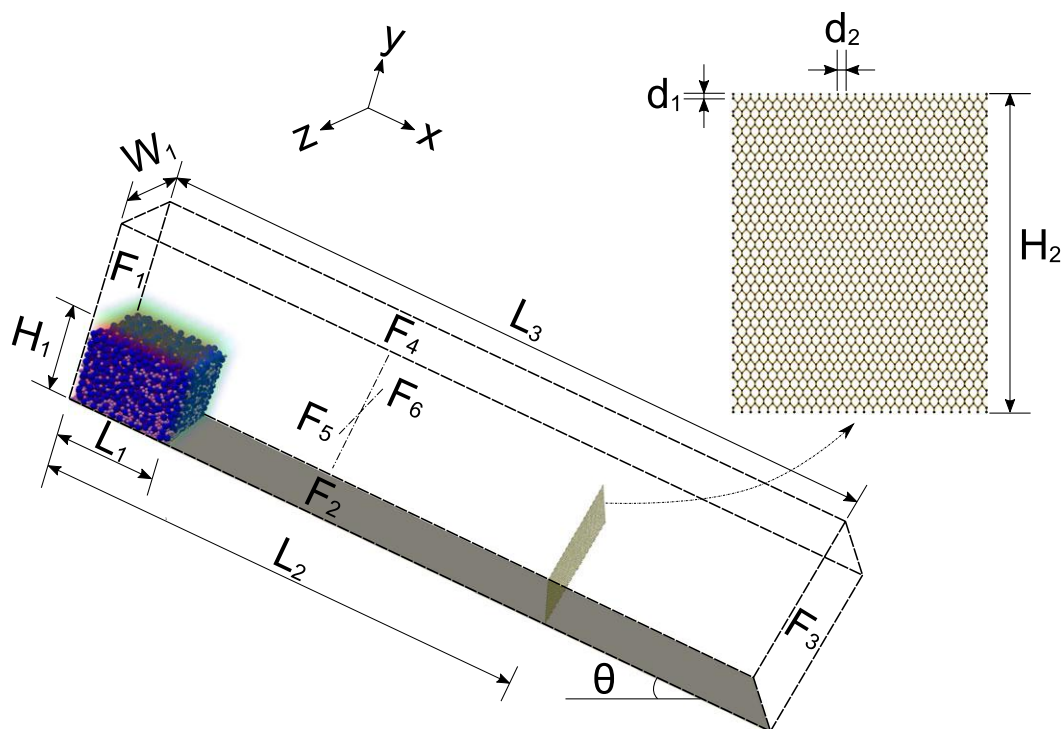
FIGURE 4 Model setup for a coupled computational fluid dynamics and discrete element method simulation of debris flow impacting on a flexible barrier [Colour figure can be viewed at wileyonlinelibrary.com]

and water (L_1, W_1, H_1) is initially placed on the top of the slope channel before being released to impact on the flexible barrier. The particulate system is a packing of bi-dispersed particles (see detail in Table 1). In the DEM simulation, 4 channel boundaries F_1, F_2, F_5, and F_6 are assumed to form fixed, rigid, and frictional walls for the particles. The right and upper faces F_3 and F_4 are assumed to be empty so that any particles not retained by the barrier can exit from the simulation. The CFD domain is bounded by an atmosphere upper face F_4 (zero pressure), an outlet right face F_3 (zero velocity gradient and zero pressure gradient), and 4 no-slip boundary walls F_1, F_2, F_5, and F_6 (zero velocity and zero normal gradient for pressure).[28] At the initial state, only fluid cells in the cubic debris domain (L_1, W_1, H_1) are assumed to contain water, while the rest of the CFD fluid cells are air. Table 1 summarizes the adopted model parameters for the particulate system, the fluid, the flexible barrier as well as the controlling parameters for the simulations. The flexible barrier is placed at a distance of L_2 along the slope from the top. Both the bottom edge and the two lateral edges of the barrier are assumed to be fixed to the channel walls to mimic anchored boundary conditions.

TABLE 1 Model parameters adopted for the coupled computational fluid dynamics and discrete element method (CFD-DEM) simulations

Debris particle	Diameter[a]	0.04 m, 0.08 m
	Density	2500 kg/m^3
	Young's modulus (particle-particle contact)	70 GPa
	Young's modulus (particle-wall contact)	700 GPa
	Poisson's ratio	0.3
	Restitution coefficient	0.7
	Interparticle friction coefficient	0.7
	Particle-wall friction coefficient	0.7
Flexible barrier	Particle diameter	0.01 m
	Particle density	5300 kg/m^3
	Young's modulus (particle-barrier contact)	5 MPa
	Poisson's ratio	0.3
	Restitution coefficient	0.3
	Interparticle friction coefficient	0.7
Water	Density	1000 kg/m^3
	Viscosity	0.001 $Pa \cdot s$
Air	Density	1 kg/m^3
	Viscosity	1.48×10^{-5} $Pa \cdot s$
Geometric size	Mixture sample width W_1	1.2 m
	Mixture sample length L_1	1.2 m
	Distance from left boundary to barrier L_2	6.0 m
	Slope channel length L_3	9.0 m
	Mixture sample height H_1	1.05 m
	Vertical distance between barrier particles d_1	0.02 m
	Horizontal distance between barrier particles d_2[b]	0.04 m
Simulation control	Time step (CFD)	5×10^{-6} s
	Time step (DEM)	5×10^{-7} s
	Simulated real time	7.5 s
	CFD cell size	0.15 $m \times 0.15$ $m \times 0.15$ m

[a]A bi-disperse particle system is considered here, where the mass percentages of particles with 0.04 m diameter and 0.08 m diameter are 20% and 80%, respectively.

[b]Note that the vertical distance d_1 and horizontal distance d_2 between barrier particles are the distances between the centers of particles.

3.2 | Verifications and benchmarking

The coupled CFD-DEM method has been benchmarked in Zhao and Shan[9,10] with classic problems in soil and fluid mechanics and has been further verified for a dynamic impacting problem featuring intense particle-fluid mixing in Shan and Zhao.[8] To further verify and benchmark its predictive capability in modeling the debris flow impacting on flexible barriers, the proposed coupled CFD-DEM has been applied to simulating a number of different combinations of barrier types, slope angles, solid fractions in the debris mixture as well as the loaded cables in a nonuniform barrier. The different modeling groups are summarized in Table 2. Emphases are placed on examining two aspects of the debris flow for the uniform flexible barrier cases, namely, the slope angle and the solid fraction in debris mixture (Group I and Group II), while the influence of loading position is investigated for the nonuniform barrier case by changing the loaded cable (Group III). In particular, the deformed shape of the nonuniform flexible barrier predicted by our numerical simulations will be quantitatively compared against the experimental and analytical results by Ferrero et al.[29]

3.2.1 | Slope angle

The influence of slope angle on the impacting behavior is first examined for a uniform barrier as shown in Figure 4 and indicated as Group I in Table 2, where the barrier height $H_2 = 1.48\ m$, the solid fraction of the released debris mixture is 49.83% and the slope angle is varied from 20° to 35°. The evolution of the impact force is depicted in Figure 5 for the 4 cases of slope angle. Here, the impact force is defined by the force impacting orthogonally to the deformed flexible barrier surface according to a similar concept as used by Leonardi et al.[1] Notably, a higher slope angle generally leads to higher peak and steady-state impact forces on the flexible barrier as well as a bigger difference between the two. Since a steeper slope yields to a larger difference between potential energies of the position where the debris mixture is released and the location where the flexible barrier is fixed, it may lead to the development of higher kinetic energy

TABLE 2 Simulated groups for verification of the coupled computational fluid dynamics and discrete element method (CFD-DEM) approach

	Barrier type	Pertaining Variable	Adopted Value/Remarks
Group I	Uniform barrier	Slope angle θ (°)	20, 25, 30, 35
Group II	Uniform barrier	Solid fraction ϕ (%)	7.39, 14.78, 23.73, 33.70,
			46.13, 49.83, 55.08, 60.41
Group III	Uniform barrier	Six identical reinforcing cables	Cable No. 2, 3, & 5 (see Figure 10)
	with cables	with equal spacing	will be chosen for analysis
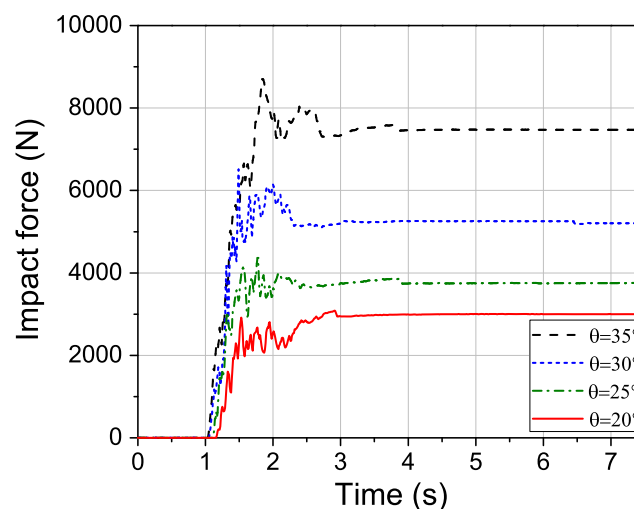
FIGURE 5 CFD-DEM predictions of evolutions of impact forces of a debris flow on a flexible barrier at different slope angles [Colour figure can be viewed at wileyonlinelibrary.com]

of the debris and hence result in a higher peak impact force, which agrees well with the experimental observations by Moriguchi et al[30] and Faug et al[31] as well as the dry DEM simulations by Albaba et al[32] and Albaba.[23] Meanwhile, the steady-state (stationary) force depends on the final retained mass in the barrier. From our simulations, it is found that a flatter slope commonly leads to more elongated deposition-shape along the sloping direction, which helps spread more weight of the final retained mass to the slope rather than having to be sustained by the flexible barrier. Consequently, the resulting steady-state force on the barrier is smaller in the flat slope case. This observation is indeed consistent with the DEM study conducted by Albaba.[23] Pertaining to the difference between the peak and steady-state impact forces, the bigger difference in a steeper slope case may imply a better mitigation effect by a flexible barrier for steeper slopes.

Figure 6A shows the evolution of the average flow velocity of the debris mixture along the flow direction x during the impacting process, indicative of two distinct stages bounded by an apparent peak in all cases. The average velocity of the debris flow features a nearly linear increase before reaching the peak (eg, at around 1.3 seconds for all cases) and then decreases substantially within 2 seconds when it impacts on the flexible barrier. The duration of impact increases with decreasing slope angle, which agrees with the observation by Albaba.[23] Furthermore, the steeper positive pre-peak and negative post-peak slopes of the high slope angle case indicate that a debris flow may be quickly accelerated once being mobilized in the presence of fluid in the mixture, and the intersecting effect of the flexible barrier is evidently effective in deaccelerating the flow, at least for the particle phase. The general trend is partially consistent with the pure DEM simulations by Albaba[23] of dry particles impacting on a flexible barrier. Nevertheless, the post-peak deacceleration rate observed by Albaba[23] is steeper than its pre-peak counterpart, while the present study observes comparable rates for
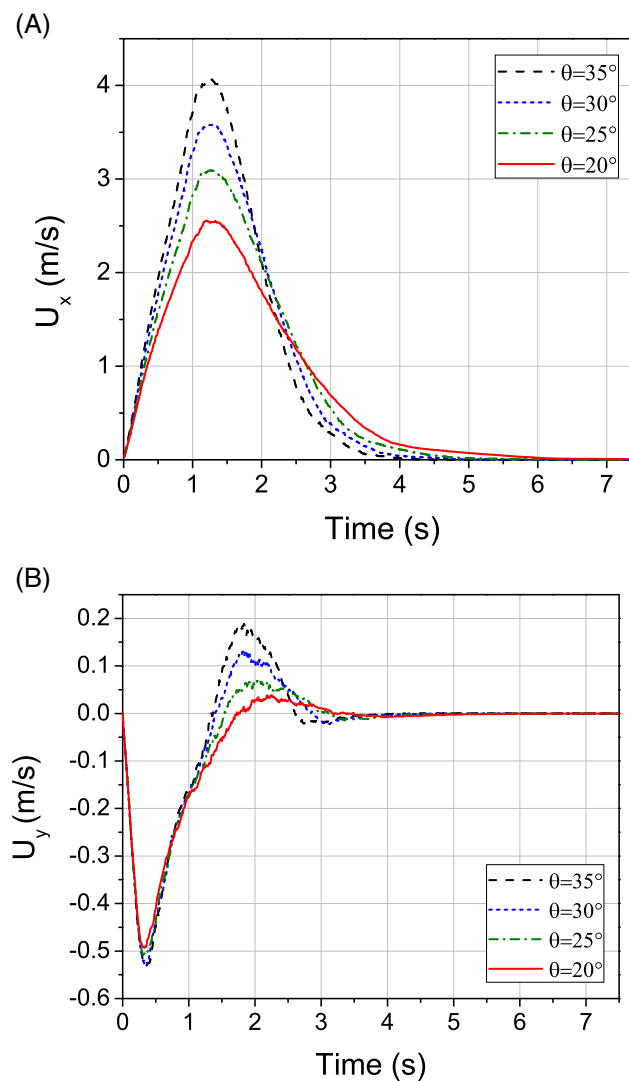
FIGURE 6 CFD-DEM predictions of the evolutions of average flow velocity along A, the flow direction x and B, the flow depth direction y [Colour figure can be viewed at wileyonlinelibrary.com]

a mixture case. Evidently, the fluid phase involving a debris mixture considered in the present study may render it more mobile than a dry particle system as treated by Albaba.[23]

The average flow velocity along the flow depth direction y is examined and shown in Figure 6B. The effects of slope angle on the maximum flow velocity and the impact duration are similar with the analysis for the average flow velocity along the flow direction x in Figure 6A. They are also consistent with the simulation data obtained by Albaba.[23] However, the negative initial flow velocity shown in Figure 6B differs apparently from the zero initial velocity in Albaba.[23] This difference is caused by the larger aspect ratio of the debris sample (sample height H_1/sample length L_1) used in our simulations. A higher debris mixture tends to collapse down along its flow depth direction first, leading to negative flow velocity in that direction.

The peak impact force is an important index for barrier design.[33-35] A popular formula for estimation of peak impact force is based on the well known hydrodynamic model which shows a positive correlation between the peak impact force and the quadratic term of the maximum flow velocity.[35] By summarizing our simulation results for the 4 slope angle cases in Figure 7, a roughly linear correlation is found between the peak impact force and the maximum flow velocity. Our positive linear correlation indeed agrees well with the observed trend by Wendeler and Volkwein[7] in their experimental results as well as Albaba[23] in the DEM simulations.
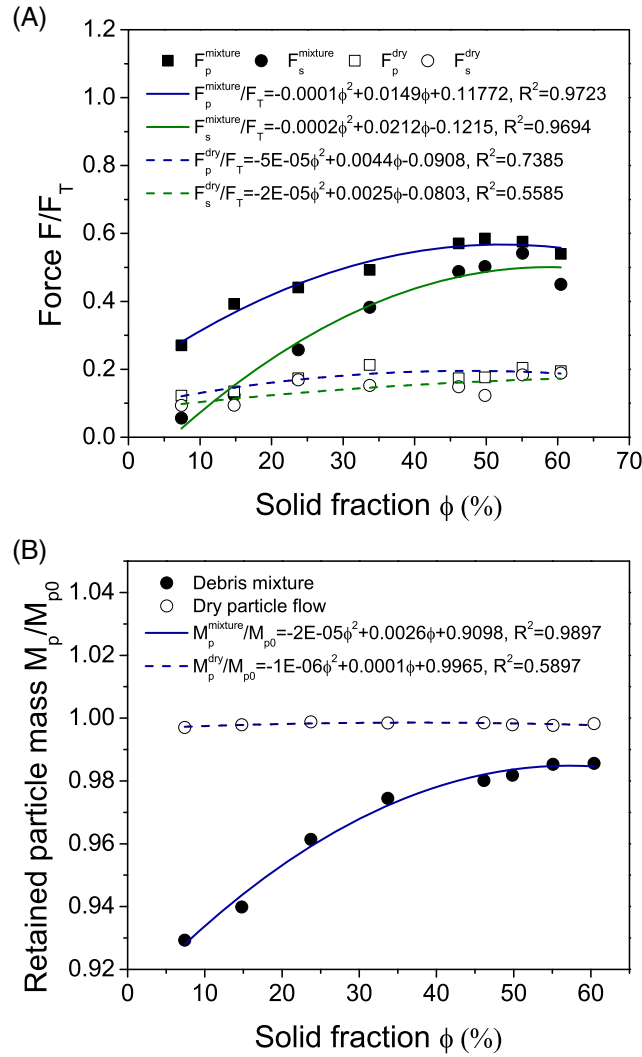
3.2.2 | Solid fraction

In Group II study, a uniform flexible barrier on a slope with fixed slope angle of 35° is considered, and the solid fraction ϕ in the released debris mixture is varied from 7.39% to 60.41% as shown in Table 2. To examine the effect of fluid on the impact behavior, comparison cases with dry particles have been simulated and the simulations results are presented in Figure 8. To make them comparable, each considered case with dry particles contains indeed exactly the same packing of particles as the corresponding debris mixture case (ie, only the fluid was removed). In doing so, it is possible to obtain different results for the dry cases with various solid fractions.

Figure 8 shows the changes of normalized impact force (A: $F_p^{mixture}$ for peak impact force and $F_s^{mixture}$ for steady-state or stationary force by a debris mixture) and the normalized retained particle mass (B) with the solid fraction. Evidently, both quantities obtained from debris mixtures show a positive nonlinear correlation with the solid fraction, resembling the trends observed in the numerical study by Leonardi et al.[1] Interestingly, Figure 8 appears to indicate a threshold solid fraction at which both the normalized impact force and the retained mass reach a peak. A further increase in solid fraction over this threshold may possibly lead to a decrease in the normalized impact force and a seemingly saturation of normalized retained particle mass. The underlying mechanism for the threshold may be three-fold: (1) the change of

$$F_p = 3739.9\, U_x^{max} - 6783.5$$
$$R^2 = 0.982$$
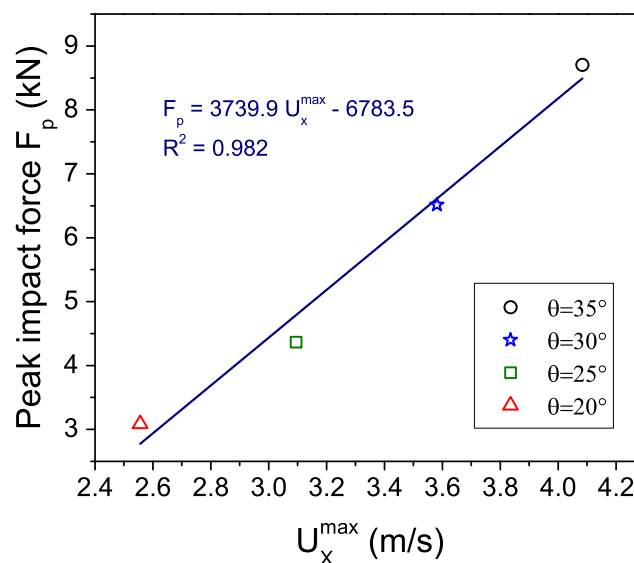
FIGURE 7 Positive correlation between peak impact force F_p and maximum flow velocity U_x^{max} [Colour figure can be viewed at wileyonlinelibrary.com]

(A)

(B)

FIGURE 8 A, Correlations of normalized impact forces and B, retained particle mass with the solid fraction of a debris mixture. In the figure, $F_p^{mixture}$ and F_p^{dry} denote the peak impact forces by a debris mixture and a dry granular flow, respectively; $F_s^{mixture}$ and F_s^{dry} are the stationary forces in mixture and dry cases; F_T is the static force ($F_T = m_T g \sin\theta$, where m_T is the total mass of mixture, and g is the gravitational acceleration). M_{p0} is the initial particle mass; $M_p^{mixture}$ and M_p^{dry} are the final retained masses in mixture and dry cases. For a mixture case with certain solid fraction, the corresponding dry flow case has the same packing of particles without any fluid [Colour figure can be viewed at wileyonlinelibrary.com]

barrier permeability, (2) a stabilized debris deposition structure retained by the barrier, and (3) the competition between debris mobility versus its density.

(1) Barrier permeability: In cases of solid fraction below the threshold, with continuous impacting and depositing of debris particles onto the barrier, the increase in particle retention will gradually reduce the overall permeability of the retained debris-barrier body, causing less passing of both fluid and fine particles. Leonardi et al[1] indeed mentioned that debris flow with higher solid fraction could result in quicker reduction of the barrier permeability, leading to increased peak and stationary forces. Evidently, the reduction rate of barrier permeability cannot keep increasing infinitely with solid fraction. When the threshold solid fraction is reached, a minimum overall permeability could possibly be reached for the captured debris-barrier body, just as a typical stable porous granular mass. With a steady permeability reached, the overall flow and impact behavior of subsequently debris will be changed, as explained below.

(2) The formation of a stabilized dead-debris-barrier structure will render less materials pass through the composite structure, but divert the majority of subsequent debris to overflow. The formation of such a dead zone serves as a cushion to reduce and even avoid further impacts being felt by the barrier directly (it may partially direct the

impact to the channel bed/walls though). The overall impact force thus will not further increase. The dead-zone structure is relatively stable, so the retained mass in the barrier becomes steady too.

(3) In addition to the above two aspects, the solid concentration of a debris also affects its impact behavior on a barrier, via an interesting competing mechanism between its relative mobility and debris density. Higher solid fraction may generally increase the flow density but decrease the flow velocity for a debris.[36] Since the impact force has been found positively correlated with both flow density and flow velocity,[37] the increase of solid fraction may thus affect impact force in a complicated manner. At relatively low solid fraction below the threshold, the increase in solid components in the debris mixture may result in increased average density without significantly slowing down the flow mobility. Hence, large impact forces are found with increased solid fraction. When the solid fraction reaches or exceeds the threshold, the overall mobility of the debris mixture may be significantly reduced. This effect may eventually reach equilibrium with the enhanced effect by the increase in debris density, causing a steady impact force on the barrier as observed in our study.

Our numerical study shows the threshold solid fraction is around 55%. Evidently, the value is dependent on our model setups, including the barrier shape, opening size, the slope angle and particle size distribution. The general validity of the above findings may need further experimental verifications.

In addition, Figure 8A clearly shows that the peak impact forces exerted by debris mixtures are higher than that by the corresponding dry granular flows, indicating an apparent enhanced mobility of overall flow by the presence of fluid. This observation agrees well with the numerical study by Leonardi et al.[1] Moreover, our simulation data show that the retained particle mass in the mixture case is always smaller than that in the corresponding dry case (see Figure 8B), but the resultant stationary forces in most mixture cases ($\phi \geqslant 14.78\%$) are higher than their corresponding dry cases. The seemingly contradictory observation can indeed be easily explained by the deposition shape of particles retained in the flexible barrier in the two cases, as shown in Figure 9. The retained particles in the mixture case impact more severely on the barrier, generate larger deformation at the upper portion of the barrier, and hence form a mass body that is mainly supported by the flexible barrier. In contrast, the dry case leads to a deposition which impacts more at the bottom of the barrier and has the majority of its weight supported by the channel. There are two cases ($\phi = 7.39\%$) where the stationary force in the mixture case is smaller than that in the corresponding dry case, which may be caused by the significant smaller retained mass in the mixture case as shown in Figure 8B. The notable differences between the mixture and dry cases observed in Figure 8B highlight the significant effect of fluid in a debris flow simulation and the necessity to include it in the consideration of debris-structure interactions. Indeed, our observation indicates if the effect of fluid is not considered in a debris, the impacts and damage to a flexible barrier may often be significantly underestimated, which may result in unsafe design.

3.2.3 | Uniform mesh with reinforcing cables subjected to out-of-plane load

Group III considers a uniform wire mesh reinforced by a total of 6 identical cables arranged with equal vertical spacing (1 m as shown in Figure 10) and explores their mechanical responses under out-of-mesh-plane loads applied to different levels of cables. An identical problem has been experimentally and analytically examined by Ferrero et al,[29] which serves as an excellent example for calibration purposes. Note that a hexagonal mesh has been used in our study instead of the ring elements in Ferrero et al.[29] While different mesh shapes may cause different barrier responses, the effect will be explored in a future work. As shown in Figure 10, the two lateral short edges of the wire mesh are fixed. Each cable is modeled as a series of extra reinforcing bond wires connecting the physical nodes of the same elevation in the barrier mesh. Cable No. 2, No. 3, and No. 5 have been chosen to apply a distributed load to examine the overall response of the barrier system. Nine homogeneous points of the chosen cable are selected, at each of which a 700 N concentrated force

Debris mixture   **Dry granular flow**
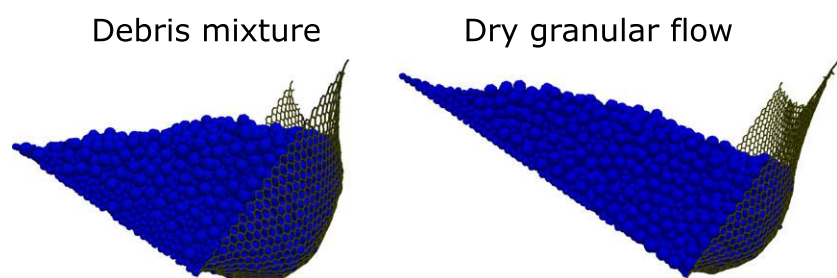
FIGURE 9 Depositions of particles after a debris mixture (left) and a dry granular flow (right) impact on a flexible barrier (for a slope angle of 35°) [Colour figure can be viewed at wileyonlinelibrary. com]
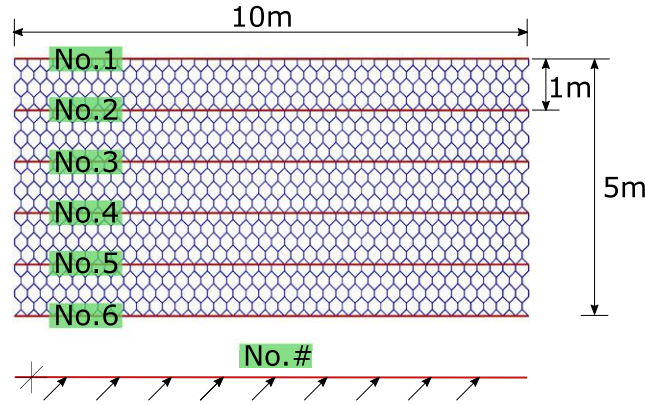
FIGURE 10 CFD-DEM modeling of a flexible barrier consisted by a uniform net and 6 cables [Colour figure can be viewed at wileyonlinelibrary.com]

is applied along out-of-plane direction of the mesh (see the illustration at the bottom of Figure 10). Only one cable is chosen for each test, and changing the loaded cable implies changed loading positions. The bond stiffnesses of the uniform mesh and the cables are calibrated to be $2 \times 10^{10} \, N/m$ and $8 \times 10^{11} \, N/m$, respectively, according to the experimental data. No debris mixture has been considered in this problem. Figure 11 compares the simulation predictions with the experimental and analytical data on the mechanical responses of the barrier system for each loading case.

Intuitively, the loaded cable sustains the largest deformation in each loading case. This is confirmed by the normalized out-of-plane displacements predicted for all cables by our DEM model in Figure 11. The same figures also present the experimental and analytical data obtained by Ferrero et al[29] for each loading case. Evidently, our DEM model predictions offer reasonable quantitative agreements with the experimental and analytical data. The observed discrepancy might be related to the different mesh shape used and the assumptions made on the constitutive law for the bond/remote interaction. Sliding effect among barrier rings and evolving stiffness of the barrier wires can be important but have been neglected in this study.

3.3 | Failure of flexible barrier

Subjected to different debris flow impacts and site conditions, a flexible barrier may potentially fail in rather different patterns. A thorough investigation of the failure of flexible barrier is critical for its practical design but may be expensive if purely relying on experiments. The proposed method in this study, in particular the use of DEM in simulating flexible barrier, offers great convenience in exploring the possible failure modes of flexible barrier under impact of debris flow. To demonstrate this, we consider the uniform barrier treated in Group I of Section 3.2.1 (the group varying the slope inclination), and fix the solid fraction and slope angle at 49.83% and 35°, respectively. The bond strength (7 ~ 25 MPa) and the bond stiffness ($1.5 \times 10^8 \sim 2.5 \times 10^8 \, N/m$) of the flexible barrier are varied to explore how they affect the failure mode.

Figures 12 and 13 summarize 4 major failure modes having been observed in our simulations. Modes I to III are characterized by the breakage of the wire mesh, while Mode IV features by excessive deformation of the barrier. As the tensile force has been normally used to capture the behavior of wires from their effective performance in sustaining the force to their failure,[11,21] the total tensile force has been investigated in Figure 13, which is defined as the vectorial sum of the tensile forces of all bonds

$$\boldsymbol{F}_t = \sqrt{\left(\sum_{i=1}^{N} \boldsymbol{F}_{ti}^x\right)^2 + \left(\sum_{i=1}^{N} \boldsymbol{F}_{ti}^y\right)^2 + \left(\sum_{i=1}^{N} \boldsymbol{F}_{ti}^z\right)^2}, \tag{24}$$

where N is the total number of the bonds, $\boldsymbol{F}_{ti}^x$, $\boldsymbol{F}_{ti}^y$, and $\boldsymbol{F}_{ti}^z$ are the components of a tensile force $\boldsymbol{F}_{ti}$ in x, y and z directions, respectively. The barrier failed in Mode I in Figure 12A breaks from the bottom to lateral edges shortly after the debris mixture collapses onto it. The initial sharp increase of the total tensile force in Figure 13 (red dash line) is caused by a sudden initial impact of the debris mixture, which leads to the breakage of the barrier from its bottom edge. As a small portion of the blocked particles are released from the broken mesh, the total tensile force drops mildly until

(A)

(B)

(C)
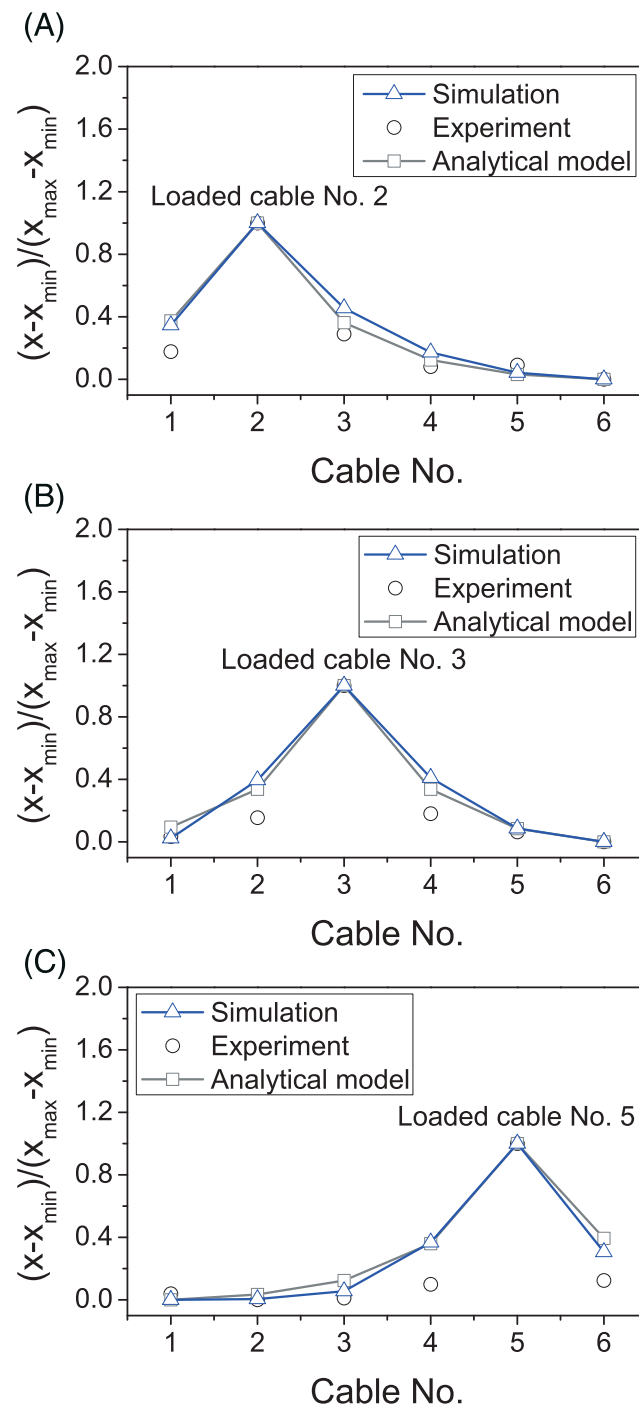
FIGURE 11 Comparison of deformed barrier shapes by experiments and analytical analyses[29] and DEM simulations with distributed loads on A, cable No. 2; B, cable No. 3; C, cable No. 5. In the figures, x is the coordinate orthogonal to the initial face of the barrier; x_{min} is the coordinate of the minimum deformed point; x_{max} is the coordinate of the maximum deformed point [Colour figure can be viewed at wileyonlinelibrary.com]

the entire bottom edge breaks. The following increase in total tensile force reflects a relatively stagnant period during which the barrier stops breaking while the clogged particle mass accumulates. The second peak corresponds to the initiation of lateral edge failure in the barrier. With the enlarging of lateral failure, more entrapped particles escape, leading to decreased tensile force. The process continues until all particles are released from the net, which results in zero tensile force in the remaining mesh. Failure mode II in Figures 12B and 13 (black solid line) depicts a continuous breakage of the mesh from its center part to around to form a major hole, during which a single peak of total tensile force is observed, corresponding to the start of the breaking. Failure mode III in Figures 12C and 13 (blue dash-dot line)
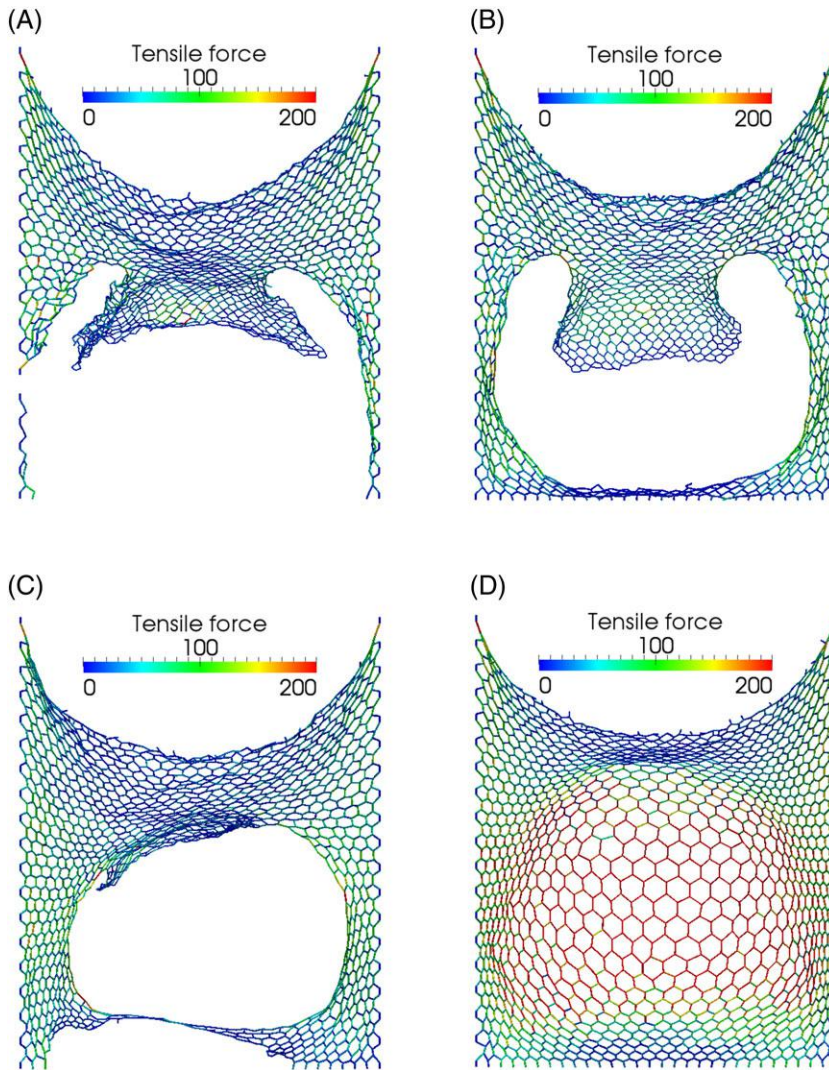
FIGURE 12 Four barriers with different failure modes: A, Mode I: Break from bottom edge to lateral edges; B, Mode II: Break from center; C, Mode III: Break from center and bottom edge simultaneously; D, Mode IV: Excessive deformation without breakage [Colour figure can be viewed at wileyonlinelibrary.com]
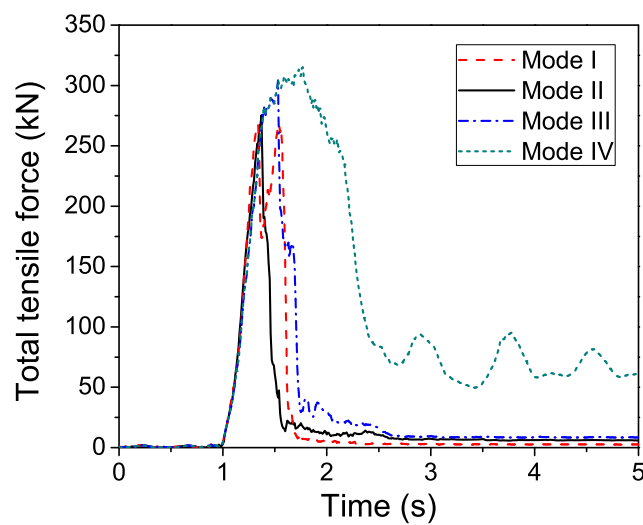
FIGURE 13 Evolution of total tensile force for four barriers suffering from various failure modes in Figure 12 [Colour figure can be viewed at wileyonlinelibrary.com]

appears to be a mixed pattern of Mode I and Mode II, whereby the barrier fails simultaneously from its bottom edge and the center part. However, our simulations indicate that this failure mode is not commonly observed. Meanwhile, the flexible barrier may also experience a failure Mode IV featured by excessive deformation without apparent breakage as shown in Figure 12D. The entire barrier network is severely stretched and the mesh openings at the center part are substantially enlarged to allow the passing of even the coarse debris particles. The first peak in the tensile force curve in Figure 13 (green short dash line) corresponds to the beginning of excessive deformation of the mesh, while the following big drop indicates a sudden substantial stretching of the entire mesh from its center by the debris impact. The successive small drops afterwards in the tail of the tensile force curve represent the combined effect of the rebounding of mesh and retained mass, the enlarging of mesh opening, and the release of part of the retained mass.

In our simulations, the bond strength has been varied from 7 MPa to 25 MPa at a fixed bond stiffness of 400 MN/m for a total of 19 cases. Figure 14 shows the evolution of total tensile force and the maximum total tensile force evolution with bond strength. Two distinctive total tensile force evolutions are found with the change of bond strength in Figure 14A. One follows a similar trend of Mode I as shown in Figure 13 with two comparable local peaks, indicative of the occurrence of breakage failure from the bottom edge to the lateral edges. The other depicts a single peak followed by fluctuations due to recursive rebounding of the debris mixture retained by the barrier, and there is no breakage occurring to the barrier, therefore the steady-state force in the barrier is not zero. Meanwhile, it is found that overtopping and releasing of coarse particles through those enlarged mesh openings contribute to a small total tensile force at a relatively steady state at $t = 5$ s. Since the same barrier stiffness has been used for all cases, all response curves follow an identical initial pre-peak path. Figure 14B clearly demonstrates the correlation between the bond strength and
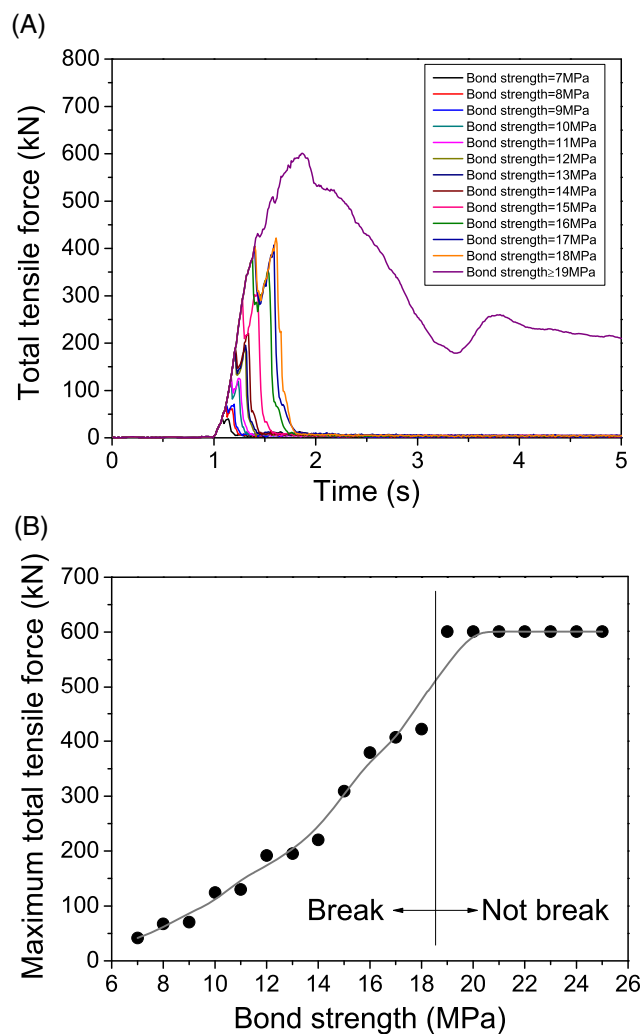
FIGURE 14 A, Evolution of total tensile force and B, variation of maximum total tensile force with bond strength [Colour figure can be viewed at wileyonlinelibrary.com]

the maximum total tensile force attainable in a flexible barrier. For cases where breakage failure occurs, the maximum total tensile force is positively correlated with the bond strength. Interestingly, the case of bond strength at 19 *MPa* appears to serve as a boundary case. No breakage is recorded and the same maximum total tensile force is found for all cases with bond strength higher than 19 *MPa*, which is consistent with the identical curves showed in Figure 14A.

The effect of bond stiffness is further examined by fixing the bond strength for the mesh. As shown in Figure 15, the evolution of the total tensile force in the barrier does not appear to show the same trend with that for the bond strength
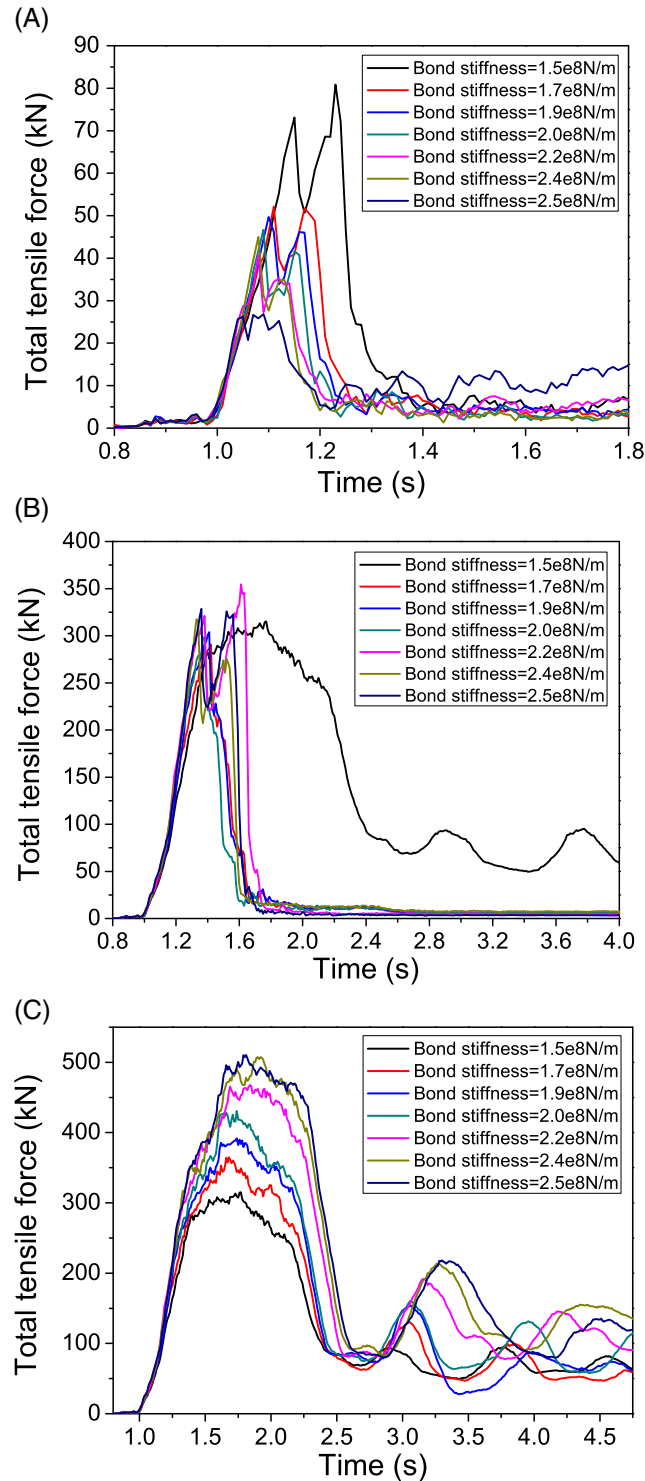
FIGURE 15 Evolution of total tensile force in the barrier at different bond stiffnesses with fixed A, bond strength = 5 *MPa*, B, bond strength = 13 *MPa*, and C, bond strength = 20 *MPa* [Colour figure can be viewed at wileyonlinelibrary.com]

in Figure 14A. Indeed, a further examination of the maximum total tensile force in Figure 16 reveals that the correlation between the maximum total tensile force and the bond stiffness is more complicated and may be totally different under different bond strength levels.
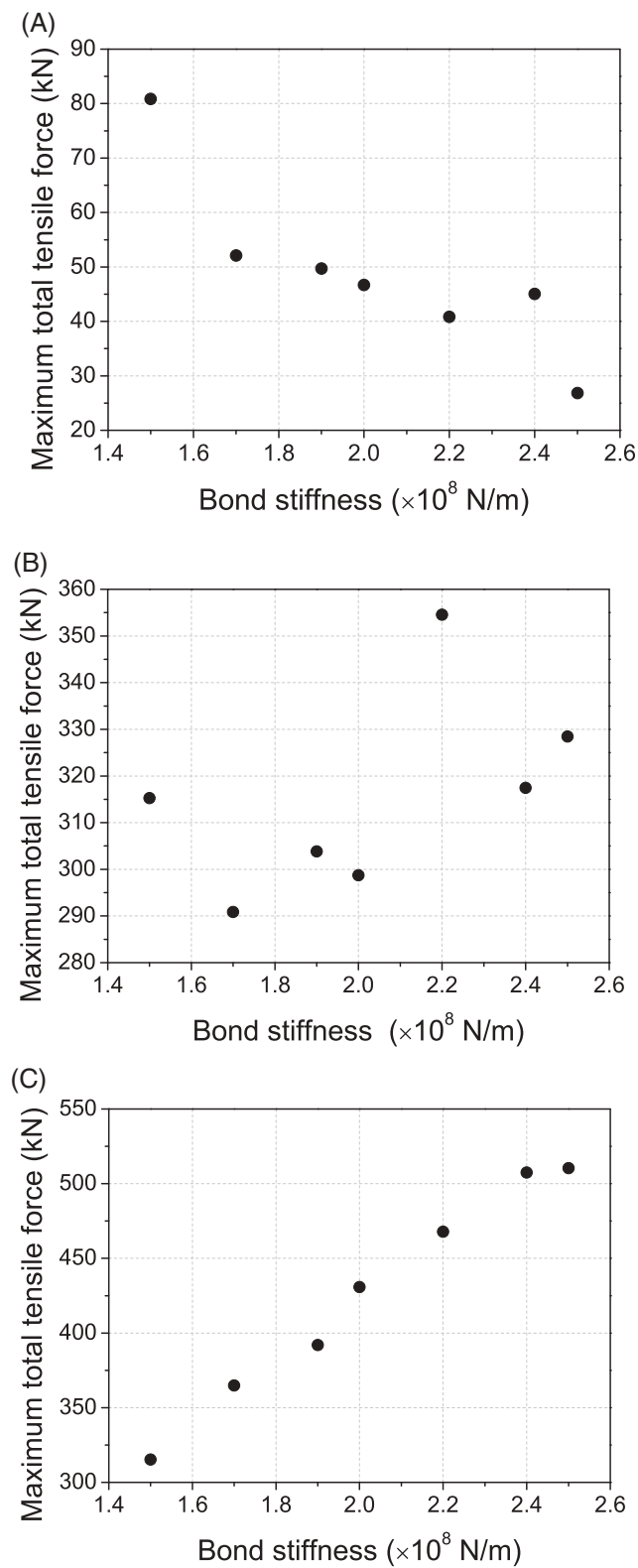
FIGURE 16 Correlation of maximum total tensile force in the barrier with bond stiffness at a fixed A, bond strength = 5 *MPa*, B, bond strength = 13 *MPa*, and C, Bond strength = 20 *MPa*

At a relatively small bond strength (eg, in the case of 5 MPa), Figure 15A illustrates that the total tensile force evolves with time according to a similar manner of Failure Mode I in Figure 13 with two comparable peaks for all cases of bond stiffness. The maximum total tensile force in Figure 16A shows a rather consistent negative correlation with the bond stiffness. Notably, the flexible barrier in some cases breaks earlier with a higher bond stiffness, leading to relatively less trapped mass and hence a smaller maximum total tensile force. At a medium bond strength (= 13 MPa), as shown in both Figures 15B and 16B, no consistent trend can be found for either the total tensile force or the maximum total tensile force. Instead, evolution curves resembling all 3 modes (I, II, and IV) can be found from Figure 15B. There is no apparent correlation identifiable between the maximum total tensile force and the bond stiffness in Figure 16B. The evolution of the total tensile force for a higher bond strength case (= 20 MPa) is shown in Figure 15C, which resembles the trend of failure mode IV where excessive deformation of the barrier mesh occurs. The maximum total tensile force is found correlated positively with the bond stiffness in this case (Figure 16C).

4 | NON-UNIFORM FLEXIBLE BARRIER REINFORCED WITH CABLES

4.1 | Non-uniform barriers with double twists and cables

Owing to its simplicity, the uniform barrier has been widely adopted for investigation in both small-scale experiments[7] and numerical simulations.[1] However, the nonuniform barrier proves to be more realistic and useful and is friendly for manufacturing as well. A nonuniform flexible barrier may consist of a systematic combination of single wires and double twists and may be further reinforced by various cables and braking elements.[4] The roles played by the various key components in mitigating debris flow impacts are important for practical design of various flexible barriers. In this section, we investigate the performance of two nonuniform flexible barriers comprised of double twists and/or reinforced by cables by considering three flexible barriers as shown in Figure 17 and described in Table 3. Barrier I is a uniform barrier consisting of single wires for comparison purpose only. Barrier II is a nonuniform barrier composed of single wires and double twists, and Barrier III is a nonuniform barrier consisting of single wires, double twists and cables. All 3 barriers have a height (H_2) of 1.06 m. The solid fraction of the debris mixture is fixed to 23.73% in all 3 cases. Based on the real properties of single wires and double twists used by Thoeni et al,[21] the bond stiffness and strength of the double twists are specified as twice of that of single wires as outlined in Table 3.

4.2 | Deformation of non-uniform flexible barriers

It is instructive to examine the deformation of the three flexible barriers to assess the effects of nonuniform components, and the comparisons are presented in Figure 18. The evolutions of maximum barrier elongation along the flow direction (x) are plotted in Figure 18A. Prior to 1 second, all 3 barriers exhibit rather similar fluctuated deformations due to the weight and the elasticity of the barrier. When they are impacted by the debris mixture, retain sufficient particles and become stabilized, all 3 barriers show quick elongations before reaching a peak along x direction. It is from the rapid deformation stage that the effects of nonuniform components are differentiated. Evidently, Barrier III presents the smallest peak and post-peak steady state elongations and Barriers II is in the middle. The mixing of double twists
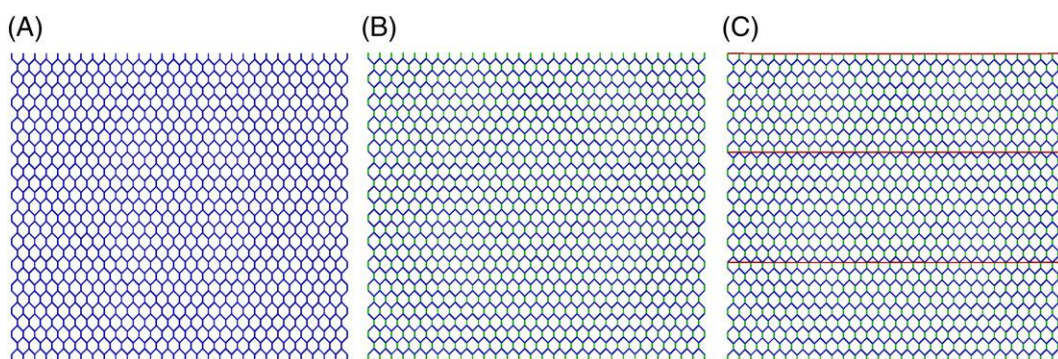
FIGURE 17 Barriers with different components: A, a uniform net (Barrier I); B, a barrier with double twists (Barrier II); C, a barrier with double twists and cables (Barrier III). Blue bonds denote single wires; Green bonds are double twists and red bonds represent cables [Colour figure can be viewed at wileyonlinelibrary.com]

TABLE 3 Barrier components and bond properties of single wires, double twists, and cables

	Number of Single wires	Number of Double Twists	Number of Cables
Barrier I	2305	0	0
Barrier II	1508	797	0
Barrier III	1508	797	3[a]
Bond stiffness (N/m)	2×10^8	4×10^8	8×10^8
Bond strength (Pa)	1×10^8	2×10^8	4×10^8

[a]Each of the horizontal cables in Figure 17 (C) is composed by 87 horizontal bonds connecting 88 barrier particles.

(Barrier II) and further use of cables (Barrier III) apparently help increase the stiffness of the barrier as compared with the uniform case (Barrier I). The same effects can be observed from the overall deformation of the barriers, shown by the deformed center span of the 3 barriers at the steady state in Figure 18B. Note that the local kink point at ($x = 6.32$ m, $y = 0.77$ m) for the case of Barrier III in Figure 18B corresponds to the position of a reinforcing cable. A further illustration of the deformed meshes (with cables, if any) for all three cases at their steady states is shown in Figure 18C, which may be compared against their deformed profile at the central spans in Figure 18B.

Evidently, the relatively larger deformation in the uniform barrier case may render at a higher risk for breakage failure. Meanwhile, excessive large deformation may also result in extremely enlarged openings for the mesh in Barrier I, which may lead to significant release of the retained debris particles and render the flexible barrier less effective. Indeed, our numerical simulations show that Barrier I retains 91.82% of the total particle mass, which is the smallest of all compared with the 92.24% for Barrier II and 96.84% for Barrier III. The exploitation of reinforcing cables in Barrier III notably enhances the retaining capacity of the barrier, and hence its effectiveness.

4.3 | Force analysis for the flexible barriers

Other than deformation, it is critical to evaluate the total force sustained by a flexible barrier. The total force is calculated by the Euclidean norm of forces over all virtual wires (bonds) throughout a barrier. Figure 19 presents the calculation results for the 3 cases. Evidently, without extra reinforcements, the uniform barrier (Barrier I) has to sustain the largest peak force as well as steady-state force, while the peak force in Barrier III is apparently smaller than the other two cases due to the help of cables. Interestingly, at steady states, Barrier II and Barrier III appear to reach roughly the same total force. Note that the occurrence of peak forces in all 3 cases coincides well with that for the maximum elongation showed in Figure 18A.

Nonuniform barriers with cables can apparently reduce the peak impacts and hence the risk of breakage for a flexible barrier. There are at least two possible underlying mechanisms accountable for the observations. Firstly, compared with the uniform barrier, the use of double twists and further cables help to enhance the stiffness of the barrier system, which leads to a reduced overall mesh deformation and a changed overall shape of the retained mass. The topological change of the retained mass may further lead to different force distribution to the slope surface and the barrier. For example, a less deformed mesh may form a retained mass with more forces shared by the slope surface than the barrier system. Second, a stiffer barrier system in cases of Barrier II and Barrier III may respond to the initial impacts of debris flow with relatively stronger rebounding, which help to push the first arriving particles towards the down flowing particles to enhance more intense mixing and energy dissipation (see also Ashwood[38]). This may account for a second mechanism for the above observations.

It is important to further identify the individual contributions of loading bearing from different components of a flexible barrier system. Figure 20 presents the loads shared by the individual components (single wires, double twists, and cables if applicable) in Barrier II and Barrier III. The insets in Figure 20 are the forces normalized with respect to the total wire number of the specific component (eg, average force per wire/bond). In a nonuniform mesh such as Barrier II and Barrier III, the nearly identical average force per wire/bond for both single wires and double twists indicates that the load is equally shared throughout the wire mesh without obvious differentiation of the nonuniformity. Notably, however, the double twists do provide higher stiffness in resisting excessive deformation as compared with a uniform single wire system, thus change the mitigation mechanisms for debris impacts. Note that the higher total force

(A)

(B)

(C)
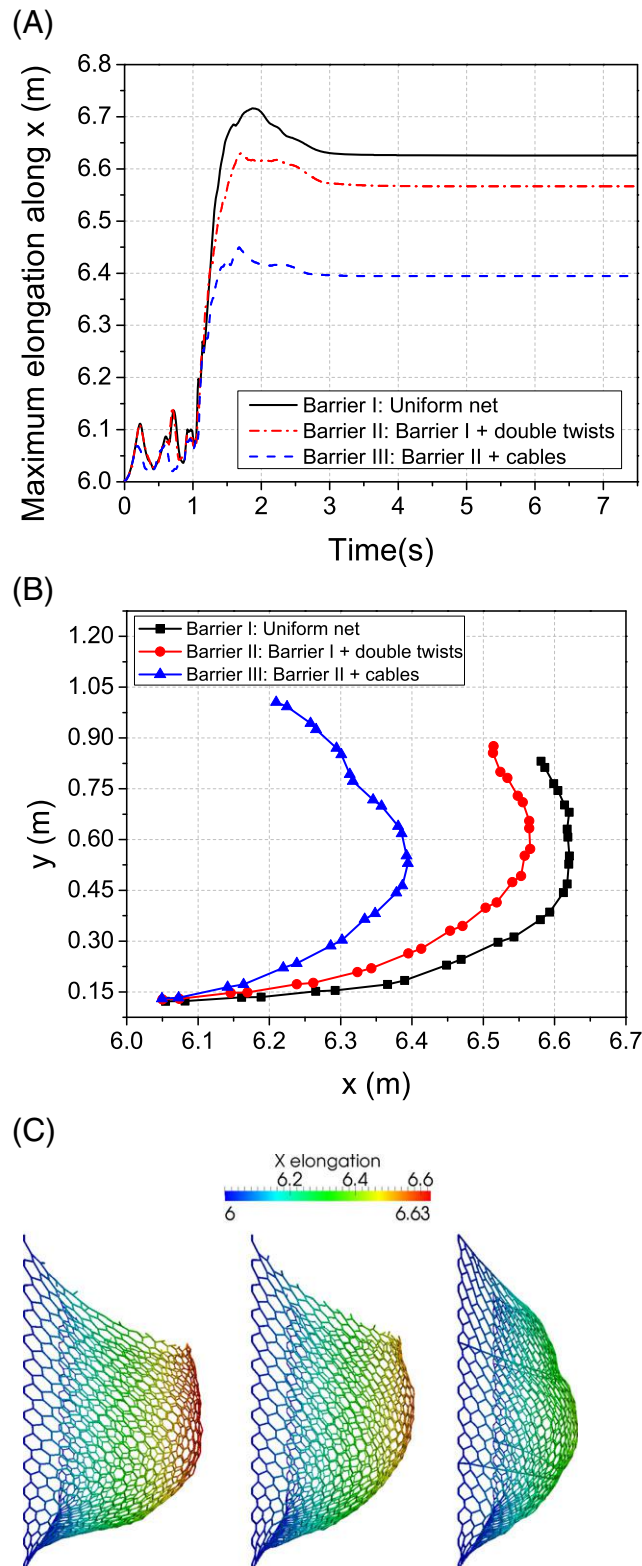
FIGURE 18 A, Evolutions of maximum barrier elongation along the flow direction x; B, deformed profiles at the center span of the barriers at their steady states; and C, side view of the deformed mesh for Barrier I (left), Barrier II (center) and Barrier III (right) at the steady state [Colour figure can be viewed at wileyonlinelibrary.com]

sustained by the single wires than the double twists shown in both figures are due to more single wires (1508 in total) than double twists (797 in total) in both barriers. When being used, each cable shares an apparently greater average force than both the single wire and double twist (Figure 20B).
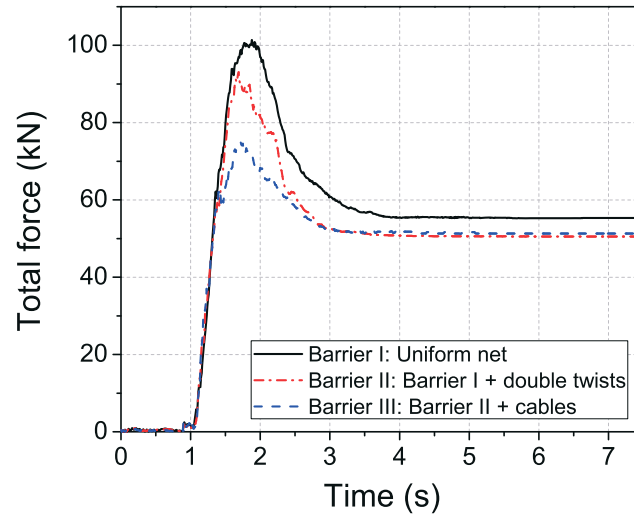
FIGURE 19 Evolution of total force sustained within barrier [Colour figure can be viewed at wileyonlinelibrary.com]
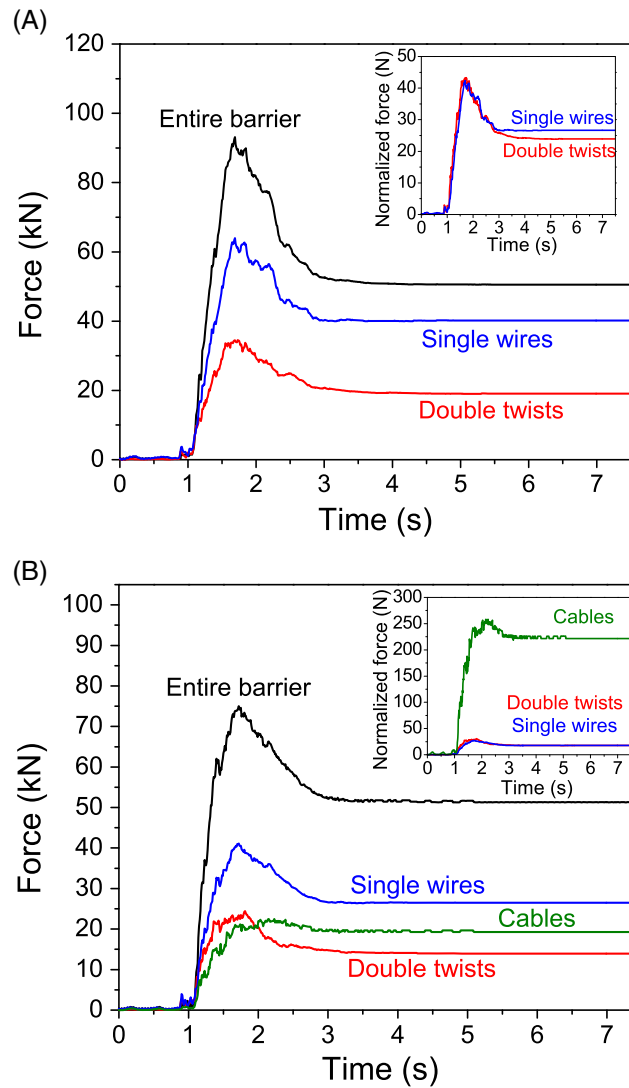

FIGURE 20 Force shared by the different components in A, Barrier II (with 1508 single wires and 797 double twists) and B, Barrier III (with 1508 single wires, 797 double twists and 3 cables) [Colour figure can be viewed at wileyonlinelibrary.com]

While the use of nonuniform double twists appears to cause rather marginal changes of force distribution within the barrier, cables can lead to substantial local redistribution of forces as well as local deformation of the barrier mesh. To understand the effects of double twists and cables on the local behavior of a flexible barrier more clearly, Figures 21 and 22 demonstrate the maximum local bond force (the force in the most critical bond/wire) and pertaining component sustaining this force. The maximum local bond force in Barrier II shown in Figure 21 does not differ much from that in Barrier I during the impacting process (prior to 2.2 s), but the stationary force at the steady state is slightly smaller in Barrier II than that in Barrier I.

Figure 22 further distinguishes the location of maximum local force during the impacting process for Barrier II. The maximum local force is found to occur in the double twists from $t = 1.0\,s$ to $t = 2.25\,s$, corresponding to the period from the inception of sudden pre-peak increase to the end of the major post-peak drop of force. During this intense impacting period, the double twists are more prone to fail than the single wires. At all other stages of the impact, however, the maximum local forces are found to occur in the single wires, including the final steady state. In particular, further inspections (see insets in Figure 22) of the simulation results show that during the dynamic impact, the maximum local forces appear at the lower center of the barrier and are sustained by vertical double twist wires. Nevertheless, in the final stationary state, the maximum local forces indeed occur in the single wires close to the two top corners of the mesh aligning with the stretching direction of the deformed mesh. These force distributions, which show that the center
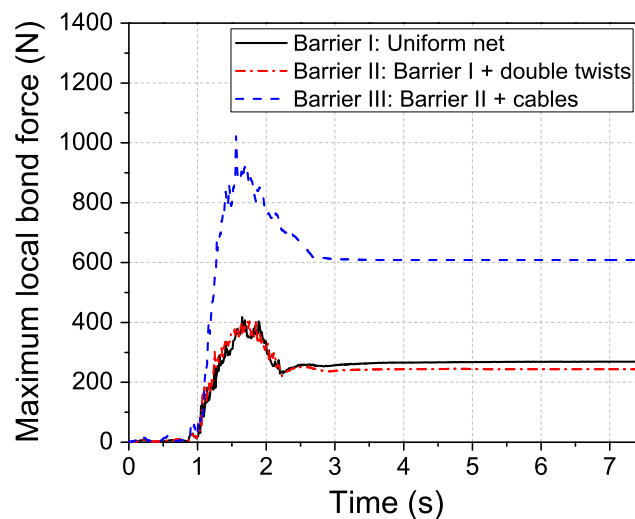
FIGURE 21 Evolution of maximum bond forces within three barriers [Colour figure can be viewed at wileyonlinelibrary.com]
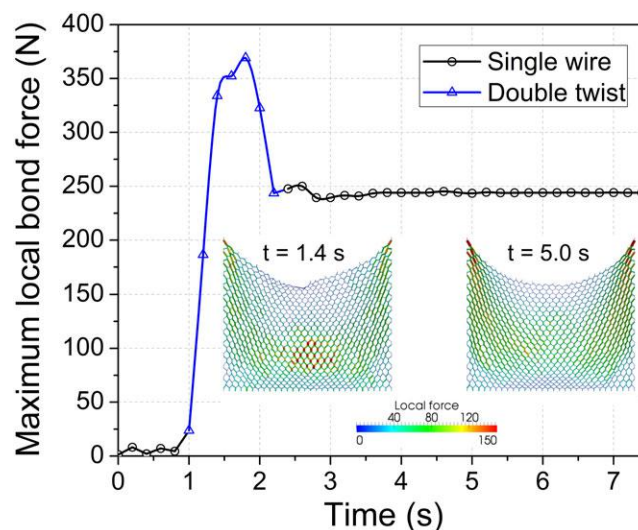
FIGURE 22 Evolution of maximum bond force and the component sustaining it in Barrier II (Barrier consisting of single wires and double twists) [Colour figure can be viewed at wileyonlinelibrary.com]
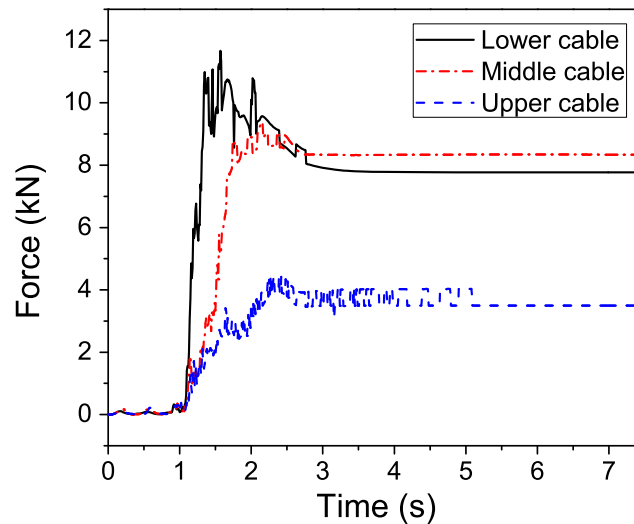
FIGURE 23 Evolution of forces of cables in Barrier III (Barrier with double twists and cables) [Colour figure can be viewed at wileyonlinelibrary.com]

and top corners of the barrier are vulnerable parts, are similar to the distribution of stretching energy shown by Leonardi et al[1] in their FEM modeling of flexible barriers.

In the presence of cables in Barrier III, as already shown in Figure 20B, the cables support the highest averaged/normalized load throughout the impacting process. It is interesting to find that the maximum local force almost exclusively occurs in the cable wires too. Although the fundamental mechanisms have yet to be figured out for the above observations, it is believed that the relative stiffness among the different components in a barrier system and the permanent deformation of the mesh may be the controlling factors. Further studies are still needed in this regard.

Three cables with equal vertical spacing have been considered in Barrier III. It is of importance to identify the critical cable(s) that sustain the highest load during and after the debris flow. Figure 23 shows the force evolutions of the 3 cables in Barrier III during the entire impacting process, which can be better correlated with the deformation process of the barrier mesh for analysis. The lower cable appears to feel the initial impact by the debris earlier than the other two, showing a quick increase in sustained force from $t = 1.1\ s$ before reaching a highest peak amongst the three cables at $t = 1.5\ s$. This indeed is consistent with several early experimental observations.[4,39,40] With further retention of debris in the barrier mesh and increased deformation of the entire mesh, the middle and upper cables also start to be tightened with increased loads. The middle level reaches a peak about 30% smaller than that in the lower cable at around $t = 2.1\ s$, while the upper cable reaches a peak only around 1/3 of that in the lower cable at around $t = 2.4\ s$. The lower cable shows the highest slope of pre-peak curve and the upper cable shows the least. At steady state, however, the middle cable exhibits a larger elongation than the other two to accommodate the overall deformation of the mesh, and thus bears the highest steady load among the three. The lower cable shows a slightly smaller deformation and steady-state force than the middle one. To sum up, the lower cable may have to be considered as the most critical one in practical design, due to its heavy load to share in sustaining the initial impacting force. The middle-level cable should also be carefully designed due to their high responsibility in sustaining the final deformation and steady-state load. Note that in the above study of Barrier III, the barrier has been designed to be high enough and there is no obvious overtopping. The load sharing among the different cables can be different if overtopping occurs. Nevertheless, the various numerical observations should be rigorously corroborated with carefully designed laboratory experiments (such as the recent study by Song et al[41]) and field tests in a future study.

5 ⏐ CONCLUSIONS

The impact of debris flow on flexible barriers has been investigated by a novel numerical framework based on discrete modeling of solid, fluid and structure interactions. A coupled CFD-DEM approach is used in this framework, where both the debris particles and the flexible barrier(s) are modeled by the DEM and the debris fluid by the CFD. Based on the same solution scheme in DEM, the solid phase in a debris mixture are modeled in a routine way in most

DEM studies as rigid particles governed by interparticle contacts and frictions, while various components in a flexible barrier, including single wires, double twists and cables, can be conveniently simulated by discrete particles with remote interactions. Within the framework, the debris particles can interact with the flexible barrier particles through collisional contacts and frictions, and all these particles are interacted with the fluid phase in the debris mixture by considering typical solid-fluid interaction forces such as drag force. As such, the complicated 3-way interactions in a typical debris mixture impacting on flexible barrier problem can be modeled in a unified, straightforward manner.

The proposed unified approach has been demonstrated to be capable of capturing the typical behavior of debris flow impacting on both uniform and nonuniform flexible barriers. The predictions are found in good accordance with experimental results, theoretical predictions and other numerical studies. The study has also examined the possible failure modes a flexible barrier may experience subjected to debris impacting and the individual performance of different components in a flexible barrier. In particular, through a systematic parametric study, we have identified instructive correlations between the critical impact force and the controlling factors such as the solid fraction of the debris mixture, the slope angle, the strength and stiffness properties of the barrier. Four major modes of failure have been identified from our study. Three are associated with the breakage of the barrier mesh, while the fourth is pertinent to excessive deformation of the barrier. It is shown that if nonuniform components such as double twists and cables are used, they not only can help reduce the overall deformation of the barrier but also facilitate to retain more debris mass. It is found that the use of cables can be particularly useful in sharing a substantial portion of the impacting load to reduce the potential damage to the barrier mesh, and thus proves to be an effective reinforcing component for flexible barrier in debris flow mitigation.

This study showcases that the proposed CFD-DEM approach may serve as a feasible and robust analytical tool for future practical design of flexible barrier in mitigating debris flow. However, this paper remains a rather preliminary pilot study before be maturing enough for practical use. The various model ingredients all need to be rigorously calibrated and verified by carefully designed experimental tests subjected to different environmental conditions. For example, more realistic parameters of normal and shear stiffnesses/strengths for wires may be adopted for the investigation on detailed failure modes due to tension and shear. Future studies should take into account realistic features of the debris, such as non-spherical particles and/or breakable aggregates in the debris and a wider grain size distribution ranging from big boulders to fine silts, as well as possible entrainment during the debris flow. More realistic considerations of the flexible barrier system may also be made, such as the introduction of energy dissipator like brake rings.[4] In addition, the present study has considered a hexagonal shaped elementary unit for the flexible barrier.[12] It is indeed not difficult at all to adapt it to other mesh shapes by simply adjusting the position of nodal particles in the barrier mesh, such as the diamond[42] and rectangle[7] shapes.

ORCID

Jidong Zhao (iD) http://orcid.org/0000-0002-6344-638X

REFERENCES

1. Leonardi A, Wittel FK, Mendoza M, Vetter R, Herrmann HJ. Particle–fluid–structure interaction for debris flow impact on flexible barriers. *Comput Aided Civ Inf Eng.* 2016;31(5):323-333.

2. Wendeler C, McArdell B, Volkwein A, Denk M, Gröner E. Debris flow mitigation with flexible ring net barriers–field tests and case studies. *WIT Trans Eng Sci.* 2008;60:23-31.

3. Wendeler C, McArdell B, Rickenmann D, Volkwein A, Roth A, Denk M. Field testing and numerical modeling of flexible debris flow barriers. In: Proceedings of the International Conference on Physical Modelling in Geotechnics; 2006; Hong Kong, China:4-6.

4. Wendeler C, Volkwein A, Roth A, Denk M, Wartmann S. Field Measurements Numerical Modelling of Flexible Debris Flow Barriers. In: Chen C-I, Major JJ, eds. *Debris-Flow Hazards Mitigation. Mechanics, Prediction, and Assessment.* Rotterdam: Millpress; 2007:681-687.

5. Canelli L, Ferrero A, Migliazza M, Segalini A. Debris flow risk mitigation by the means of rigid and flexible barriers-experimental tests and impact analysis. *Nat Hazards Earth Syst Sci.* 2012;12(5):1693.

6. Volkwein A, Wendeler C, Guasti G. Design of Flexible Debris Flow Barriers. In: 5Th International Conference Debris-Flow Hazard Mitigation. Mechanics, prediction and assessment; 2011; Padua, Italy:1093-1100.

7. Wendeler C, Volkwein A. Laboratory tests for the optimization of mesh size for flexible debris-flow barriers. *Nat Hazards Earth Syst Sci.* 2015;15(12):2597-2604.

8. Shan T, Zhao J. A coupled CFD-DEM analysis of granular flow impacting on a water reservoir. *Acta Mech.* 2449;225(8):2014.

9. Zhao J, Shan T. Coupled CFD–DEM simulation of fluid–particle interaction in geomechanics. *Powder Technol.* 2013;239:248-258.

10. Zhao J, Shan T. Numerical modeling of fluid-particle interaction in granular media. *Theor Appl Mech Lett.* 2013;3(2):021007.

11. Bertrand D, Nicot F, Gotteland P, Lambert S. Discrete element method (DEM) numerical modeling of double-twisted hexagonal mesh. *Can Geotech J.* 2008;45(8):1104-1117.

12. Thoeni K, Giacomini A, Lambert C, Sloan SW, Carter JP. A 3D discrete element modelling approach for rockfall analysis with drapery systems. *Int J Rock Mech Min Sci.* 2014;68:107-119.

13. Cundall PA, Strack OD. A discrete numerical model for granular assemblies. *Gé,otechnique.* 1979;29(1):47-65.

14. Li X, Zhao J. Numerical simulation of dam break by a coupled CFD-DEM approach. *Jpn Geotech Soc Spec Publ.* 2016;2(18):691-696.

15. Koch DL, Hill RJ. Inertial effects in suspension and porous-media flows. *Annu Rev Fluid Mech.* 2001;33(1):619-647.

16. O'Sullivan C. *Particulate Discrete Element Modelling: A Geomechanics Perspective.* Hoboken, NJ: Taylor & Francis; 2011.

17. Zhu H, Zhou Z, Yang R, Yu A. Discrete particle simulation of particulate systems: theoretical developments. *Chem Eng Sci.* 2007;62(13):3378-3396.

18. Bokkers G, van Sint Annaland M, Kuipers J. Mixing and segregation in a bidisperse gas–solid fluidised bed: a numerical and experimental study. *Powder Technol.* 2004;140(3):176-186.

19. Li J, Kuipers J. Gas-particle interactions in dense gas-fluidized beds. *Chem Eng Sci.* 2003;58(3-6):711-718.

20. Nicot F, Cambou B, Mazzoleni G. Design of rockfall restraining nets from a discrete element modelling. *Rock Mech Rock Eng.* 2001;34(2):99-118.

21. Thoeni K, Lambert C, Giacomini A, Sloan SW. Discrete modelling of hexagonal wire meshes with a stochastically distorted contact model. *Comput Geotech.* 2013;49:158-169.

22. Potyondy D, Cundall P. A bonded-particle model for rock. *Int J Rock Mech Min Sci.* 2004;41(8):1329-1364.

23. Albaba A. Discrete Element Modeling of the Impact of Granular Debris Flows on Rigid and Flexible Structures. *PhD thesis*: Université Grenoble Alpes; 2015.

24. Bertrand D, Nicot F, Gotteland P, Lambert S. Modelling a geo-composite cell using discrete analysis. *Comput Geotech.* 2005;32(8):564-577.

25. Hearn G, Barrett RK, Henson HH. Development of effective rockfall barriers. *J Transp Eng.* 1995;121(6):507-516.

26. Mustoe G, Huttelmaier H. Dynamic simulation of a rockfall fence by the discrete element method. *Comput Aided Civ Inf Eng.* 1993;8(6):423-437.

27. Thoeni K, Lambert C, Giacomini A, Sloan S, et al. Discrete Modelling of a Rockfall Protective System. In: Onate E, Owen R, eds. *Particle-Based Methods - Fundamentals and Applications.* Drodrecht, Netherlands: Springer; 2011:24-32.

28. Biscarini C, Di Francesco S, Manciola P. CFD Modelling approach for dam break flow studies. *Hydrol Earth Syst Sci.* 2010;14(4):705.

29. Ferrero A, Segalini A, Umili G. Experimental tests for the application of an analytical model for flexible debris flow barrier design. *Eng Geol.* 2015;185:33-42.

30. Moriguchi S, Borja RI, Yashima A, Sawada K. Estimating the impact force generated by granular flow on a rigid obstruction. *Acta Geotech.* 2009;4(1):57-71.

31. Faug T, Caccamo P, Chanut B. Equation for the force experienced by a wall overflowed by a granular avalanche: experimental verification. *Phys Rev E.* 2011;84(5):051301.

32. Albaba A, Lambert S, Nicot F, Chareyre B. Relation between microstructure and loading applied by a granular flow to a rigid wall using DEM modeling. *Granul Matter.* 2015;17(5):603-616.

33. He S, Liu W, Li X. Prediction of impact force of debris flows based on distribution and size of particles. *Environ Earth Sci.* 2016;75(4):298.

34. Huang HP, Yang KC, Lai SW. Impact force of debris flow on filter dam. *Momentum.* 2007;9(2):03218.

35. Scheidl C, Chiari M, Kaitna R, et al. Analysing debris-flow impact models, based on a small scale modelling approach. *Surv Geophys.* 2013;34(1):121-140.

36. Huo M, Zhou Jw, Yang Xg, Zhou Hw. Effects of a flexible net barrier on the dynamic behaviours and interception of debris flows in mountainous areas. *J Mt Sci.* 2017;14(10):1903-1918.

37. Hübl J, Suda J, Proske D, Kaitna R, Scheidl C. Debris Flow Impact Estimation. In: Proceedings of the 11Th International Symposium on Water Management and Hydraulic Engineering; 2009; Ohrid, Macedonia:1-5.

38. Ashwood W. Numerical Model for the Prediction of Total Dynamic Landslide Forces on Flexible Barriers. *PhD thesis*: University of British Columbia; 2014.

39. Bugnion L, Wendeler C. Shallow landslide full-scale experiments in combination with testing of a flexible barrier. *WIT Trans Eng Sci*. 2010;67:161-173.

40. Ng CWW, Song D, Choi C, Koo R, Kwan J. A novel flexible barrier for landslide impact in centrifuge. *Gé,otechnique Lett*. 2016;6(3):221-225.

41. Song D, Choi C, Ng CWW, Zhou G. Geophysical flows impacting a flexible barrier: effects of solid-fluid interaction. *Landslides*. 2017:1-12.

42. Volkwein A, Roth A, Gerber W, Vogel A. Flexible rockfall barriers subjected to extreme loads. *Struct Eng Int*. 2009;19(3):327-332.